

## Key Points:

- InSight landed within a 27-m-diameter, 0.3-m-deep, degraded impact crater called Homestead hollow
- Homestead hollow has a maximum age of 400 to 700 Myr. Degradation rates were two orders of magnitude higher in first 50 Myr after impact
- Homestead hollow is filled with up to 3 m of loose infill that is composed of sand and pebbles. The hollow fill is capped by a duricrust

## Correspondence to:

N. H. Warner,  
warner@geneseo.edu

## Citation:













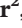




Warner, N. H., Grant, J. A., Wilson, S. A., Golombek, M. P., DeMott, A., Charalambous, C., et al (2020). An impact crater origin for the InSight landing site at Homestead hollow, Mars: Implications for near surface stratigraphy, surface processes, and erosion rates. *Journal of Geophysical Research: Planets*, 125, e2019JE006333. <https://doi.org/10.1029/2019JE006333>

Received 13 JAN 2020

Accepted 5 MAR 2020

Accepted article online 31 MAR 2020

# An Impact Crater Origin for the InSight Landing Site at Homestead Hollow, Mars: Implications for Near Surface Stratigraphy, Surface Processes, and Erosion Rates

N. H. Warner<sup>1</sup> , J. A. Grant<sup>2</sup> , S. A. Wilson<sup>2</sup> , M. P. Golombek<sup>3</sup> , A. DeMott<sup>1</sup> , C. Charalambous<sup>4</sup> , E. Hauber<sup>5</sup> , V. Ansan<sup>6</sup> , C. Weitz<sup>7</sup> , T. Pike<sup>8</sup> , N. Williams<sup>3</sup> , M. E. Banks<sup>8</sup> , F. Calef<sup>3</sup> , M. Baker<sup>2</sup> , M. Kopp<sup>1</sup> , M. Deahn<sup>1</sup> , H. Lethcoe<sup>3</sup> , and L. Berger<sup>3</sup> 

<sup>1</sup>Department of Geological Sciences, 1 College Circle, SUNY Geneseo, Geneseo, NY, USA, <sup>2</sup>Center for Earth and Planetary Studies, Smithsonian National Air and Space Museum, Washington, DC, USA, <sup>3</sup>Jet Propulsion Laboratory, California Institute of Technology, Pasadena, CA, USA, <sup>4</sup>Department of Electrical and Electronic Engineering, Imperial College London, London, UK, <sup>5</sup>German Aerospace Center (DLR), Institute of Planetary Research, Berlin, Germany, <sup>6</sup>Laboratory of Planetary Geodynamics, University of Nantes, Nantes, France, <sup>7</sup>Planetary Science Institute, Tucson, AZ, USA, <sup>8</sup>NASA Goddard Space Flight Center, Greenbelt, MD, USA

**Abstract** The InSight mission to Mars landed within *Homestead hollow* on an Early Amazonian lava plain. The hollow is a 27-m-diameter, 0.3-m-deep quasi-circular depression that shares morphologic and sedimentologic characteristics to degraded impact craters. Unlike the intercrater plains outside of the hollow, the interior lacks cobbles and is dominated by loose sand, granules, and pebbles. Fresher craters near the landing site exhibit meter-scale bedforms in their ejecta and on their floors due to sediment trapping. The sedimentology of the interior fill of *Homestead hollow* suggests similar trapping. The hollow falls along a morphologic continuum that requires low rates of rim degradation and fill. Crater degradation rates (rim erosion plus filling) in the landing site decline nonlinearly through time from  $10^{-2}$  to  $10^{-4}$  m/Myr as craters evolve to a hollow-like form. Rim erosion rates are lower initially, at  $10^{-3}$  m/Myr, but converge with degradation rates to  $10^{-4}$  m/Myr. This implies that while filling plays an important role soon after crater formation, it is limited in later stages. Crater statistics indicate that the bulk of the fill occurred in the first ~50 Myr for *Homestead hollow*. The estimated maximum age of the hollow is ~400 to 700 Myr. This requires near-zero fill aggradation and long-term soil stability for the bulk of the crater's history. Fill stability manifests in *Homestead hollow* as a ~5- to 10-cm-thick duricrust, formed by exchanges of atmospheric water vapor with soil. The estimated degradation in the hollow requires ~2 to 3 m of sedimentary fill beneath the lander.

**Plain Language Summary** The Interior Exploration using Seismic Investigation, Geodesy and Heat Transport (InSight) mission to Mars landed in western Elysium Planitia. The landing site consists of a smooth, flat surface that is unique relative to the surrounding rockier plains. Observations from orbital satellite imagery indicate that InSight landed inside of an almost circular depression in the landscape. Here we evaluate the shape and form of this small circular depression and compare it against nearby degraded impact craters. We conclude that InSight landed inside a very old crater that has filled in with windblown sediment and slope debris from the crater wall. We also estimate that the crater has been sitting on the landscape, experiencing extremely slow degradation, for approximately 400 to 700 Myr. The crater origin for the depression has implications for our understanding of the materials that exist immediately beneath the lander and the results from the two geophysical instruments onboard InSight, the Seismic Experiment for Interior Structure (SEIS) and Heat Flow and Physical Properties Package (HP<sup>3</sup>).

## 1. Introduction

The Interior Exploration using Seismic Investigation, Geodesy and Heat Transport (InSight) mission to Mars (Banerdt et al., 2020) landed in western Elysium Planitia at 4.502°N, 135.623°E on a regolith-covered basaltic lava plain and within a ~0.3-m-deep, ~27-m-diameter quasi-circular feature that is informally named

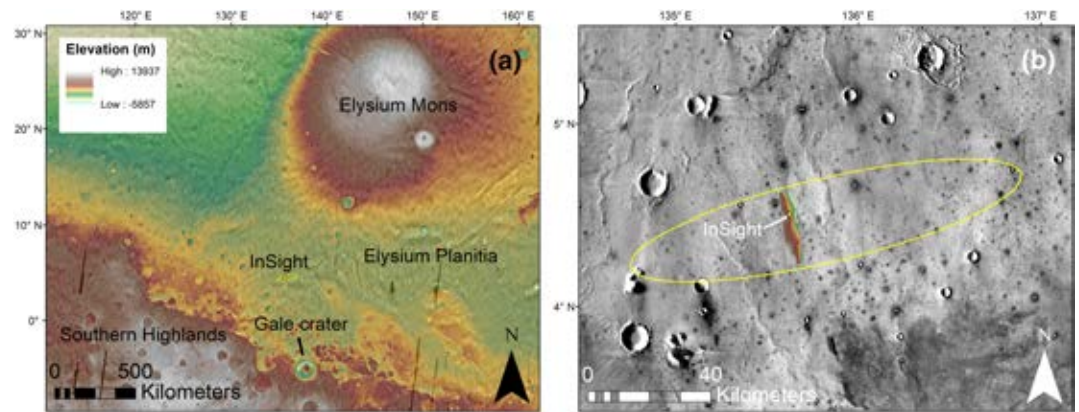


**Figure 1.** (a) Mars Orbiter Laser Altimeter (MOLA) color-shaded digital elevation model overlain on the Thermal Emission Imaging System (THEMIS) daytime infrared (IR) mosaic showing the regional context of the InSight landing site in western Elysium Planitia. (b) Zoomed in view of the THEMIS daytime IR mosaic showing the final orientation of InSight's landing ellipse, the footprint of the High Resolution Imaging Science Experiment (HiRISE) stereo image pair and DEM, and the location of the InSight lander (dot). North-south trending wrinkle ridges cross the landing ellipse. The thermal signature of the landing site suggests a geologically uniform, sand-dominated, regolith-covered plain (Golombek et al., 2017). Dark (cold in daytime IR) halos surrounding 100-m to 2-km diameter impact craters indicate rocky ejecta.

*Homestead hollow* (Figures 1–3). From initial ground-based observations, including a preliminary analysis of the local geomorphology, characterization of the sedimentology of the regolith, and comparisons to similar hollows visited by the Spirit rover at Gusev crater, Golombek et al. (2020) suggested that *Homestead hollow* is a highly degraded impact crater. Here we test the impact crater hypothesis for *Homestead hollow* and other heavily degraded, hollow-like landforms proximal to the InSight landing site. We utilize available images from the High Resolution Imaging Science Experiment (HiRISE) camera and a derived digital elevation model (DEM) to quantify the spatial distribution and morphometry of all impact structures and hollows within a  $\sim 21\text{-km}^2$  region surrounding the lander. We hypothesize that if the hollows, and by extension *Homestead hollow*, are heavily degraded impact structures, then their size-frequency distribution (SFD) and morphometry should be consistent with crater production and degradation given the observed and inferred surface processes and estimated degradation rates. Previous work established a crater classification system, constrained the degradation processes, and estimated crater degradation rates for relatively fresh, 10- to 100-m-scale craters across the entire InSight landing ellipse (Sweeney et al., 2018). This new, post-landing analysis extends that work to include more degraded craters and focuses more specifically on the lander's location and the implications for lander-scale geological/geophysical observations.

We demonstrate here that *Homestead hollow* follows the degradational continuum of craters observed throughout InSight's landing ellipse (Sweeney et al., 2018) and is of impact origin. Furthermore, we establish the SFD of all craters in the region, including and excluding the hollows. We show that the SFD that includes the hollows follows a crater equilibrium function (Hartmann, 1984) that is consistent with an impact crater population that is experiencing long term degradation by relatively steady state surface processes (e.g., eolian, impact, and mass wasting processes).

An impact crater origin for *Homestead hollow* has important implications for our understanding of the near surface stratigraphy and degradation history of the immediate location surrounding InSight as well as the broader region. Using known depth to diameter relationships and the crater retention age of  $\sim 25\text{-m}$ -size craters, we predict the initial morphometry of the hollow, the depth of infilling materials, and estimate a rate of degradation. Furthermore, the data allow us to constrain the origin of the local materials and the stratigraphic architecture of the upper few meters of the regolith. The Heat Flow and Physical Properties Package (HP<sup>3</sup>) (Spohn et al., 2018), designed to measure the heat flux of the planet, has resumed its percussive hammering into the local soil as of writing this paper. The instrument requires unconsolidated regolith for successful penetration, with a maximum penetration depth of  $\sim 5$  m. Furthermore, HP<sup>3</sup> hammering acts as an active seismic source. Monitoring of the shallow seismic signals by the Seismic Experiment for Interior

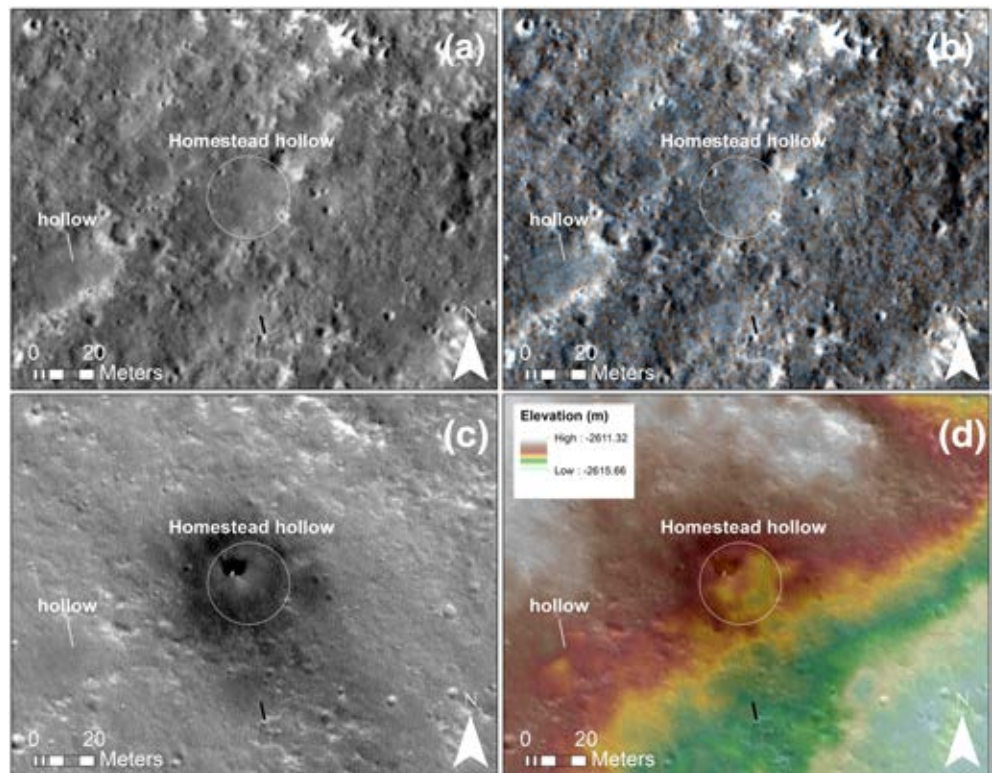


**Figure 2.** (a) Pre-landing High Resolution Image Science Experiment (HiRISE) image ESP\_036761\_1845\_RED (25 cm per pixel) showing the location and outline of *Homestead hollow*. Another quasi-circular hollow, located ~33 m to the southwest, is labeled for comparison. It shares similar geomorphologic, color, and topographic characteristics to *Homestead hollow*. (b) RGB composite HiRISE image showing color variations between the intercrater plains, which contain a generally higher abundance of cobble-size basaltic clasts, and the smooth interior materials at *Homestead hollow*. The rockier materials have a slightly lower albedo and have a red-brown hue in this enhanced color stretch. Hollow floor materials are generally higher in albedo and are less red in this stretch. (c) Post-landing HiRISE image ESP\_058005\_1845 showing the location of the InSight lander relative to the boundaries of *Homestead hollow*. The center of the lander is ~6.5 m from the northwest boundary of the rim. (d) HiRISE 1-m DEM (InSightE17\_C1) showing the hollow's topographic characteristics. *Homestead hollow* is a semi-enclosed, ~0.3-m-deep topographic depression with a possible preserved rim structure along its southern margin. Illumination is from the left.

Structure (SEIS), and derivation of wave velocities, provides a constraint on material properties and regolith thickness (Kedar et al., 2017) that can be tested against geologic observations. Early results suggest a low seismic velocity zone beneath the lander that corresponds with at least 1 m of porous, granular material (Lognonné et al., 2020). A higher velocity zone is indicated beneath these depths indicating coarser materials. Finally, landscape degradation rates are used here to evaluate local surfaces processes with implications for the geomorphic evolution of regolith-covered lava plains elsewhere on Mars.



**Figure 3.** Instrument Deployment Camera (IDC) partial mosaic (~290° azimuth around lander) of the InSight landing site. Mosaic ID LRGB\_0014\_RAS030100CYL\_R\_SCIPANQM1. The approximate border of *Homestead hollow* is illustrated with a dashed line. The azimuth (in degrees) and compass directions of this view are also shown. A distinct sedimentologic dichotomy exists between the materials within the hollow and the surrounding intercrater plains. The surficial soils in the hollow are sand-dominated with granules, pebbles and only occasional cobbles (~2% cumulative fractional area of rocks). Cobbles near the center of the hollow show evidence for partial burial (Grant et al., 2020, this issue). Cobbles on the intercrater plains are generally perched above the soil. *Rocky Field* has a relatively higher concentration of pebble to cobble size float rocks that may drape the western rim of the hollow and postdate its formation (Grant et al., 2020, this issue).

### 1.1. Geologic Context and Background

Pre-landing orbital investigations of InSight's 130 × 27 km landing ellipse (Figure 1) indicated a smooth, regolith-covered lava plain across the entire landing region (Golombek et al., 2017, 2018; Warner et al., 2017), including the location surrounding *Homestead hollow*. Regional geologic mapping identified this portion of western Elysium Planitia as part of the Early Hesperian transitional unit (eHt), comprised of layered volcanic and/or sedimentary materials (Tanaka et al., 2014). Pre- and post-landing geomorphic, thermal, and mineralogic observations support a basaltic volcanic origin (Golombek et al., 2018; Pan et al., 2019). North-south trending wrinkle ridges, 10- to 100-m-diameter (order of magnitude) rocky ejecta craters (RECs), degraded lobate flow margins, and spectra consistent with mafic minerals at shallow depths (exposed in fresh crater walls), have all been identified within the immediate region surrounding and including the landing ellipse (Golombek et al., 2018; Pan et al., 2019). Impact crater statistics using the SFD of craters between 200 m and 1 km in diameter suggest an Early Amazonian resurfacing age that is likely associated with regional Amazonian volcanism (Warner et al., 2017).

Post-landing observations of the hollow and the exterior plains from the Instrument Deployment Camera (IDC) and Instrument Context Camera (Maki et al., 2018) onboard InSight confirm orbital observations (Golombek et al., 2020). InSight rests on a smooth, poorly sorted, regolith-covered plain dominated by sand-size particles with a low abundance of meter-size rocks (~1% to 2% cumulative fractional area; Golombek et al., 2020; Charalambous et al., 2019; Grant et al., 2020, this issue; Figures 3 and 4). The dominant modification processes that likely operated on this terrain include impact cratering, mass wasting, and eolian processes. Several meter-size impact craters and dust-covered eolian bedforms are within view of the lander. There is no intact bedrock visible. The observed float rocks are likely ejecta, delivered to this location by impacts. Pebble to boulder-size clasts in the regolith are angular to sub-angular, fine-grained, and dark gray (Golombek et al., 2020; Weitz et al., 2019; Grant et al., 2020, this issue; Figures 4a and 4b). The texture, fabric, and color of these clasts are consistent with aphanitic basalt. Proximal to the lander (within ~1 to 3 m), reddish-brown, equant, sub-angular to sub-rounded, mostly pebble-size clasts are present. These are interpreted to be clods of weakly cohesive duricrust that were excavated, along with loose sand, granules, and pebble-size basaltic clasts, by the lander's pulsed retro-rockets (Golombek et al., 2020; Ansan et al., 2019; Figures 4c and 4d).

Two notable surface types are present in view of the lander and are defined by a variation in the abundance and size-frequency of clasts. These terrain types include a smoother terrain that occurs within the boundaries of *Homestead hollow* and a rockier terrain that occurs at the edge and beyond the hollow boundaries (Figures 2–4). The view south, southeast, and east from the lander, within approximately 15 to 20 m, is dominated by granular, sand to pebble-size materials (Figures 3 and 4). Sand grains are not resolvable in the highest resolution IDC images (1 mm per pixel; Maki et al., 2018) but are inferred by both orbital thermal inertia (Golombek et al., 2017) and ground-based thermal inertia derived from the onboard Radiometer experiment (Mueller et al., 2019; Golombek et al., 2020). A microns-thick dust layer was likely present but has since been removed by the lander rockets (Ansan et al., 2019; Williams et al., 2019). The smooth surface generally lacks cobble-size materials.

From available HiRISE images at 25 to 30 cm per pixel (McEwen et al., 2007) and a 1-m DEM, the smooth interior of *Homestead hollow* corresponds with a ~27-m-wide, ~0.3-m-deep, quasi-circular depression. (Figure 2). The lander rests entirely within the northwest margin of this depression. A transition between the smooth, hollow-interior materials, and a rockier-terrain-dubbed *Rocky Field* occurs to the southwest (Golombek et al., 2020; Grant et al., 2020, this issue; Figure 3). Pebble-size clasts and a few cobbles from this rock field occur along the western edge of the instrument deployment workspace. The rocks drape the hollow's margin and superpose the smooth surface suggesting that their emplacement postdates the hollow (Grant et al., 2020, this issue). IDC images taken immediately west, northwest, and north of the lander also reveal a rocky terrain outside of the hollow. The rock abundance is more consistent here with the intercrater plains across the landing region (~2–4% cumulative fractional area; Golombek et al., 2020). Several cobble-size rocks at the transition of the hollow interior and the rocky exterior show evidence for partial burial by hollow-interior materials, evidenced by embayment of rocks at their base by fines (Grant et al., 2020, this issue). The number of buried rocks abruptly decreases at the edge of the hollow where rocks are instead perched on top of the granular regolith. This suggests that the smooth material in the hollow is a fill that buried a preexisting rockier surface.

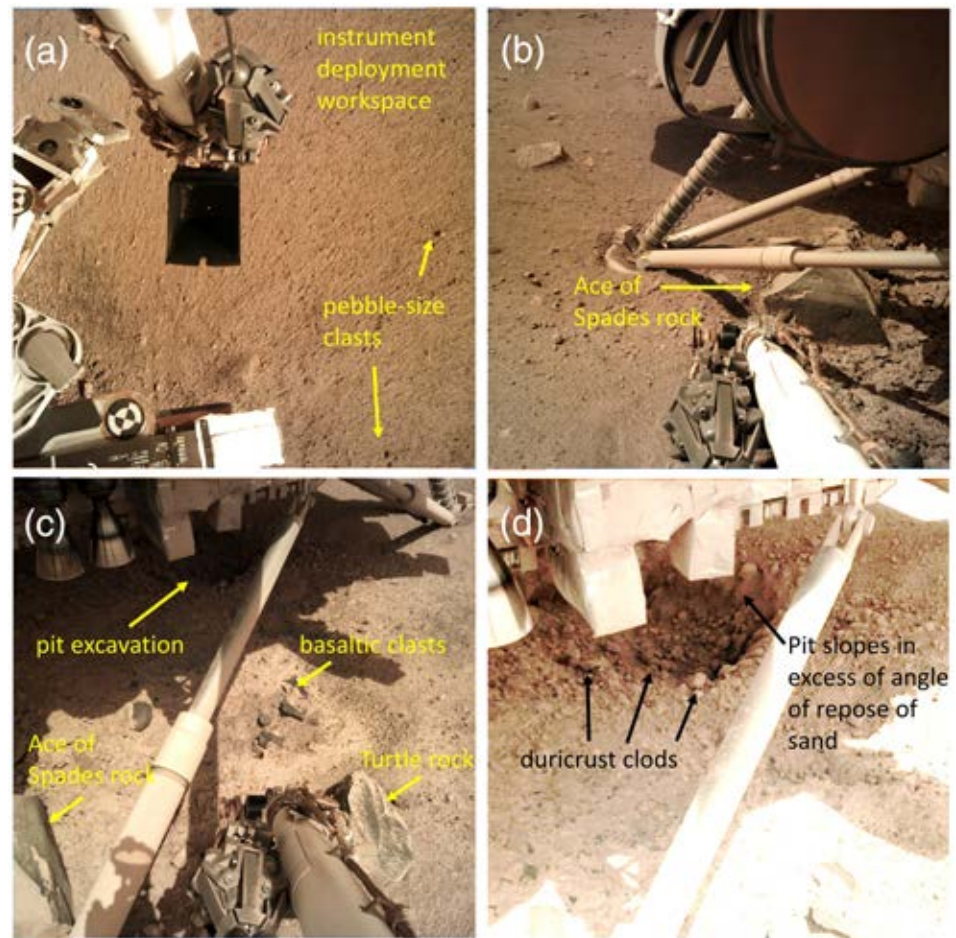


**Figure 4.** (a) Instrument Deployment Camera (IDC) image D000M0008\_597249416EDR\_F0000\_0554M of the workspace south of the lander taken on Sol 8. This area is characteristic of the smooth material inside of *Homestead hollow*, containing abundant sand (inferred from orbital and ground-based thermal inertia, Golombek et al., 2020), granules, and pebble-size materials. Resolution of the raw images range from approximately 1 to 2 mm per pixel. (b) IDC image D000M0014\_597773743EDR\_F0000\_0127M taken on Sol 14 looking immediately beneath the lander at the southwest footpad. A large, boulder-size float rock dubbed *Ace of Spades* is adjacent to the footpad. The texture and color of this rock is consistent with aphanitic basalt. Triangular facets may indicate eolian abrasion. (c) Sol 18 IDC image D002R0018\_598131254EDR\_F0707\_0010M taken immediately beneath the lander showing the margin of *Ace of Spades*, a fluted rock called *Turtle rock*, and a ~10-cm-deep pit excavated by the landers retro-rockets. A cluster of coarse, pebble-size, basaltic clasts are also indicated. (d) A zoomed and contrast-stretched version of the same IDC image taken on Sol 18 showing the morphology and sedimentology inside of the pit. Pit walls appear to exceed the angle of repose of sand (with no obvious debris aprons), consistent with the presence of a duricrust within the upper ~5 to 10 cm of the regolith. Equant, reddish-brown, duricrust clods were excavated by the rockets. Preservation of the clods through ejection out of the pit suggests some cohesion.

A few boulder-size rocks, including *First rock* and *The Pinnacles*, are within view to the south and north of the lander, respectively (Golombek et al., 2020). *Ace of Spades rock*, a ~30-cm-diameter, angular aphanitic basaltic block, rests immediately below the lander and was partially exhumed from the granular regolith by the lander rockets (Figures 4b and 4c). The angular facets of this rock suggest the possibility of eolian abrasion, which may have occurred in situ or before the rock was ejected to this location. Other venticated rocks in view of the lander include *Turtle rock* (Golombek et al., 2020; Figure 4c).

The sedimentologic observations of *Homestead hollow* and the terrain surrounding InSight are consistent with the preferential preservation/accumulation of fines within a topographic depression (Grant et al., 2020, this issue). Further, the dominance of sand-sized clasts suggests eolian transport into the hollow. Multiple meter to 10-m-size hollows with similarly smooth surfaces are visible from the lander, scattered

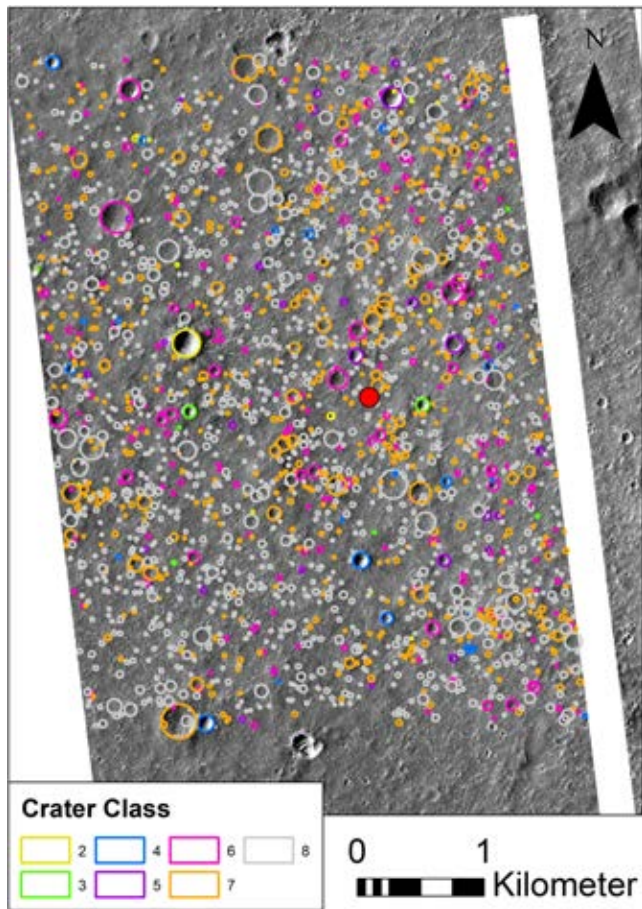


**Figure 5.** HiRISE image ESP\_036761\_1845\_RED showing the crater count and the crater classification (color-coded) for the 21-km<sup>2</sup> study area. The general location of the InSight lander is noted by a filled, red circle. All craters  $\geq 20$  m in diameter, including Class 8 hollows, are shown.

throughout the intercrater plains. Quasi-circular topographic depressions that share similar planform and topographic geomorphic characteristics to *Homestead hollow* are also abundant across the region as viewed in HiRISE images (Figures 5 and 6). These similarly quasi-circular features, range in size from 10 to 100 m in diameter, form partially enclosed meter to sub-meter-deep depressions as viewed in HiRISE DEMs and are notably smoother in appearance. All of the hollows across the landscape have a generally lower rock abundance in their interiors relative to the intercrater plains.

Hollows identified on the Hesperian-age lava plains at Gusev crater by the Spirit rover have comparable morphologic and sedimentologic characteristics to *Homestead hollow* (Golombek, Crumpler, et al., 2006; Golombek, et al., 2020; Grant et al., 2006). At Gusev, the hollows are interpreted as degraded impact craters due to their SFD relative to larger craters, their roughly circular planform morphology, and their uniquely blocky, yet planed-off rims. While similarly circular and containing dominantly finer clasts, *Homestead hollow* and nearby hollow-like features in the study region do not exhibit obvious blocky or raised rims. Alternative origins for quasi-circular hollows on regolith-covered lava plains remain implausible. Hollows may be remnant depressions inherited from original lava flow topography. Other endogenic formation mechanisms might be possible (e.g., pit formation by collapse), but such mechanisms need to account for their abundance and apparent random distribution across the landscape.

## 2. Methods

### 2.1. Crater and Hollow Mapping

To test the impact crater origin for *Homestead hollow*, all impact craters and hollow-like landforms with diameters  $\geq 20$  m were mapped within a  $\sim 21$ -km<sup>2</sup> region centered on the InSight lander (Figure 5). All available pre-landing and post-landing HiRISE data sets, including a single channel RED image at 25 cm per pixel, a DEM with 1-m grid spacing, and the cor-

responding 1-m orthorectified image, were carefully georeferenced in ArcGIS to the planet's cartographic frame using an equidistant cylindrical projection. The basemap for georeferencing included the Mars Express High Resolution Stereo Camera images (12.5 m per pixel) and CTX images (6 m per pixel) that were coregistered to the Mars Orbiter Laser Altimeter-gridded DEM (463-m postings). HiRISE image ESP\_036761\_1845 was used for the crater mapping and was acquired before landing. Surface alteration by the lander's retro-rockets precludes use of post-landing images as it obscures the subtle boundaries of the hollow (Williams et al., 2019; Golombek et al., 2020). The DEM (InSight\_E17\_C) was produced from HiRISE stereopair ESP\_036761\_1845 and ESP\_037262\_1845 (Ferguson et al., 2017).

Craters and hollows were mapped in the study region using CraterTools (Kneissl et al., 2011), a crater counting extension to ArcGIS. Each feature was mapped from rim peak to rim peak using the three-point digitization tool and the 25 cm per pixel HiRISE image. Where rims are absent or difficult to detect in the image, slope inflections in the DEM between the surrounding plains and the crater/hollow floor were used to define the boundary. In the case of the hollows, this sloping boundary is difficult to map precisely, resulting in a few meters of uncertainty in the rim boundary. In the case of *Homestead hollow*, a  $\pm 5$  m difference in measured crater diameter (25 to 30 m) exists due to rim ambiguity. We use a 27-m hollow diameter throughout the analysis (Figure 2).

### 2.2. Crater Classification Scheme

Each mapped crater or hollow was classified based on its observed state of preservation. A pre-landing crater classification scheme (Sweeney et al., 2018) identified five states (Classes 1 to 5) of preservation for only RECs across the Smooth Terrain in the landing ellipse that represent a continuum of crater degradation by surface

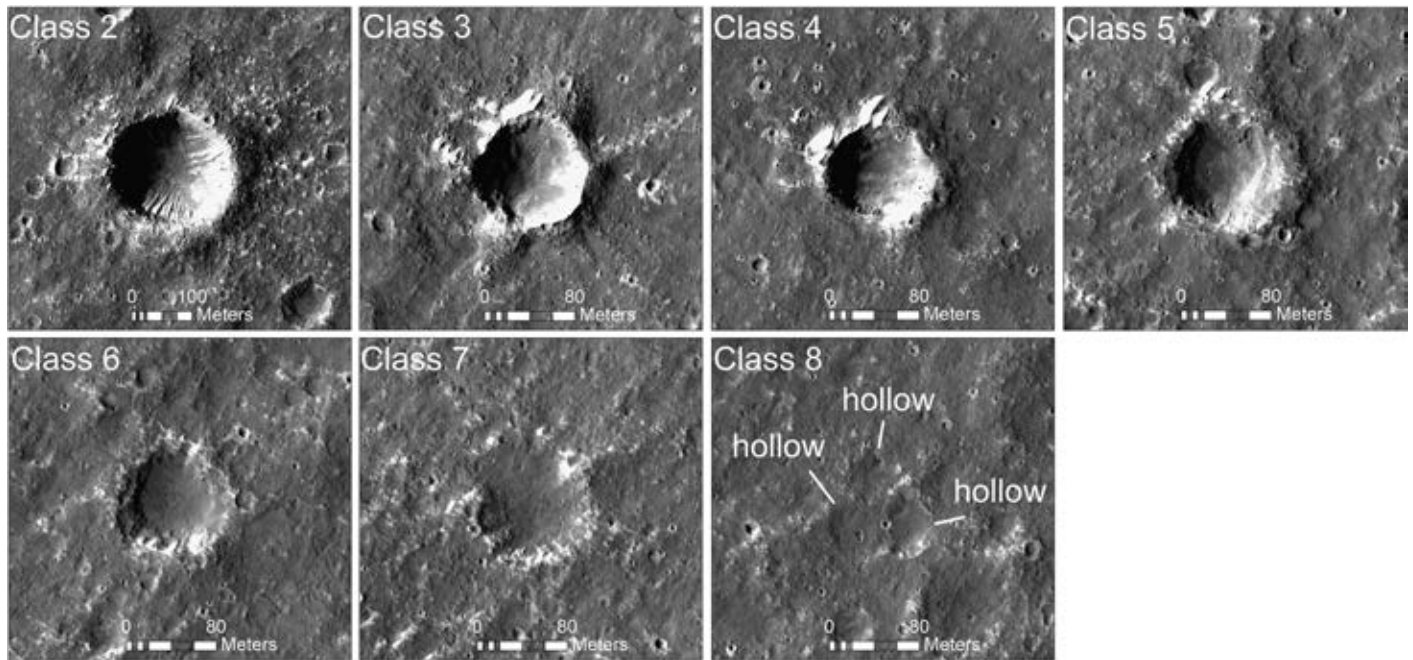


**Figure 6.** HiRISE images showing example craters in each class. The craters shown here all occur within the 21-km<sup>2</sup> study region and are proximal to the InSight lander. Class 2 craters represent the most fresh impact structures in the area. Class 8 hollows may be highly degraded impact craters. *Homestead hollow* is Class 8. Descriptions of the morphology of each class are detailed in the main body of the text. North is up and illumination is from the left.

processes through time. RECs are relatively young, 100 m to 2 km-size impact craters that excavated large, meter-size rocks from depth into their continuous ejecta blanket. The rocks are observable at HiRISE resolution and exhibit a relatively high thermal inertia in Thermal Emission Imaging System (THEMIS) data (Figure 1; Golombek et al., 2017). Class 2 craters are the most pristine, RECs in the region. Class 1 craters, although more pristine than Class 2, are generally too small to have excavated rocks. Class 5 represents the most degraded examples that still preserve rocks in their ejecta (Figure 6). The REC classification scheme was used during landing site assessment to evaluate the relative risk of landing within a rocky ejecta blanket (Golombek et al., 2017), to determine the regolith thickness from the onset diameter of rocky ejecta (Warner et al., 2017), and to constrain crater preservation timescales and erosion rates (Sweeney et al., 2018).

To summarize the Classes 1 to 5 scheme, RECs in the InSight landing ellipse degrade through a combination of filling, degradation of meter-size rocks from the ejecta blanket, rim height reduction, slope decline, and rim backwasting (Sweeney et al., 2018). The classification represents a continuum of degradation that operates over a timescale that varies depending on crater diameter. One-hundred-meter-scale craters for instance degrade from Classes 1 to 5 over time intervals that are on the order of (order of magnitude) 100 Myr, while 10-m-scale craters degrade over 10 Myr timescales (Sweeney et al., 2018). A 200-m-diameter Class 2 crater is therefore significantly older than a 20-m-diameter Class 2 crater. A 20-m-diameter Class 2 crater is younger than a 20-m-diameter Class 5 crater.

Class 1 impact features are typically (order of) 1 to 10 m in diameter and represent the ideal pristine state. Few Class 1 craters exist in the landing ellipse, owing to the relatively rapid degradation that occurs at the earliest stages of crater formation (Sweeney et al., 2018; Grant et al., 2006, 2008, 2020, this issue). There are no Class 1 craters in the 21-km<sup>2</sup> study region. Where present in the landing ellipse, they are identified by their generally low albedo ejecta (few to no ejected rocks visible at HiRISE resolution) and pristine rim structure. Their ejecta differentiates them from the similarly young (0.1–1.0 Myr) and small (1 to 10 m) Corinto crater secondaries, which have distinctly high albedo ejecta (Bloom et al., 2014; Golombek et al., 2017; Hundal et al., 2017). Most Class 1 craters and Corinto secondaries exhibit some evidence, albeit minimal, for small (sub-meter) interior bedforms.

Class 2 craters are near-pristine in morphology (Figure 6). They have well-defined continuous rims that lack notches, a continuous rocky or nonrocky ejecta blanket, sub-meter- to meter-size eolian bedforms on their

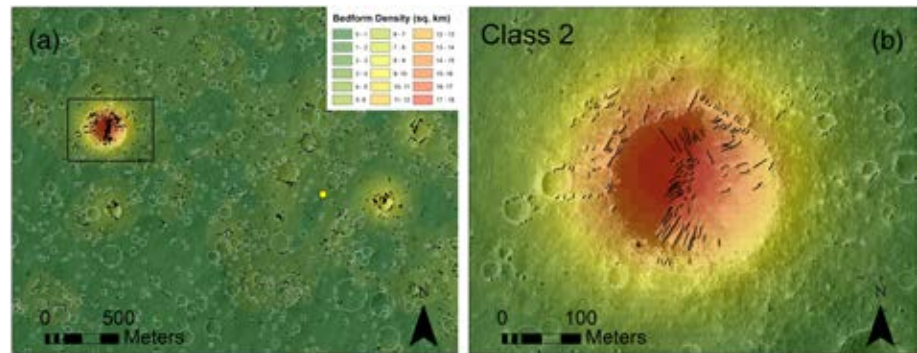


**Figure 7.** (a) Bedform (ripples and dunes) density map in the region proximal to the InSight lander. The crestlines of the bedforms are displayed as black lines. The location of the InSight lander is noted by the yellow dot. Bedforms are present, scattered throughout the continuous ejecta of craters, from Classes 1 through 3. Bedforms become increasingly concentrated against the rims of craters from Classes 2 through 5 (a few during Class 6) (Figure 6). Meter-scale bedforms are present on the floors of craters from Classes 1 to 4. During Class 4 and always by Class 5, the bedforms disappear, in favor of smoother crater fill. The intercrater plains generally lack evidence for organized sand. (b) Example Class 2 crater in the study region. Meter-scale bedforms are trapped against the outside of the crater rim and against blocks of ejecta on the northwest side of the crater. The northwest quadrant of a crater's circumference is the favored location for bedforms everywhere in the landing ellipse and are suggestive of a dominant wind direction. Bedforms on the crater floor are slightly larger, suggesting a larger volume of sand. Dune crest orientations here are also more variable, consistent with multi-directional wind patterns (swirling winds). The pattern of sand organization throughout the landing region suggests that craters are sediment traps for a somewhat limited supply of mobile sand.

crater floor (Figure 7), and similar-size bedforms trapped throughout the ejecta blanket, often against rocks. Not all fresh craters in the landing ellipse exhibit rocky ejecta. Rocks are absent in ejecta of fresh craters with diameters up to 30 to 60 m (cutoff diameter varies locally in the ellipse). A 2- to 5-m-thick loosely consolidated, sand-dominated regolith extends across the Smooth Terrain in the landing ellipse and buffers smaller impacts from reaching the deeper rockier unit (Golombek et al., 2017, 2018; Warner et al., 2017). Therefore, most Class 2 varieties at this smaller size are not RECs, including those identified in the local study region.

From Classes 3 to 5, the crater rims become more subdued and notches/superposed impacts are more common (Figure 6). The rock abundance in the ejecta (if present) decreases and the ejecta becomes less continuously distributed. Bedforms that were initially present in the ejecta are organized by Classes 3 and 5 to specific locations along the crater rim, dominantly occurring along the northwest portion of the rim (Figure 7). Bedforms in the interior of the crater also organize into larger, meter-scale features but eventually plane off to form a smooth fill unit. Classes 4 and 5 mark the transition from interior bedforms to smooth fill. The fill retains small, superposed craters (Figure 8).

The previous analyses of Classes 1 to 5 craters by Sweeney et al. (2018) confirmed that the observed degradational sequence in HiRISE images predictably tracks with the morphometry of craters as measured in the HiRISE DEM, including crater depth and rim height. Here we take a similar approach to Sweeney et al. (2018) by first classifying the craters surrounding the InSight lander and then applying a morphometric analysis to better understand the degradational sequence. However, because the initial classification only included relatively fresh, rocky ejecta examples, a revised scheme is used here that now includes more-degraded and smaller nonrocky varieties.

Class 6 craters represent impact structures that completely lack ejecta blocks at HiRISE resolution, regardless of their size (Figure 6). This generally separates them as older than Class 5. This approach is however not reliable for differentiating the two classes for craters smaller than 30 to 60 m due to the regolith buffering effect (Warner et al., 2017). Notches and gaps in the Class 6 crater rims, indicating near complete rim destruction, are evident and generally exceed ~25–50% of the total circumference. Bedforms in the ejecta are rare, but in places are trapped against the exterior of elevated rim remnants, most commonly along the northwestern quadrant (Figures 6 and 7). The crater interior exhibits a smooth, crater-retaining surface with a generally larger crater size frequency than Class 5 crater interiors (Figure 8). Only rarely are bedforms



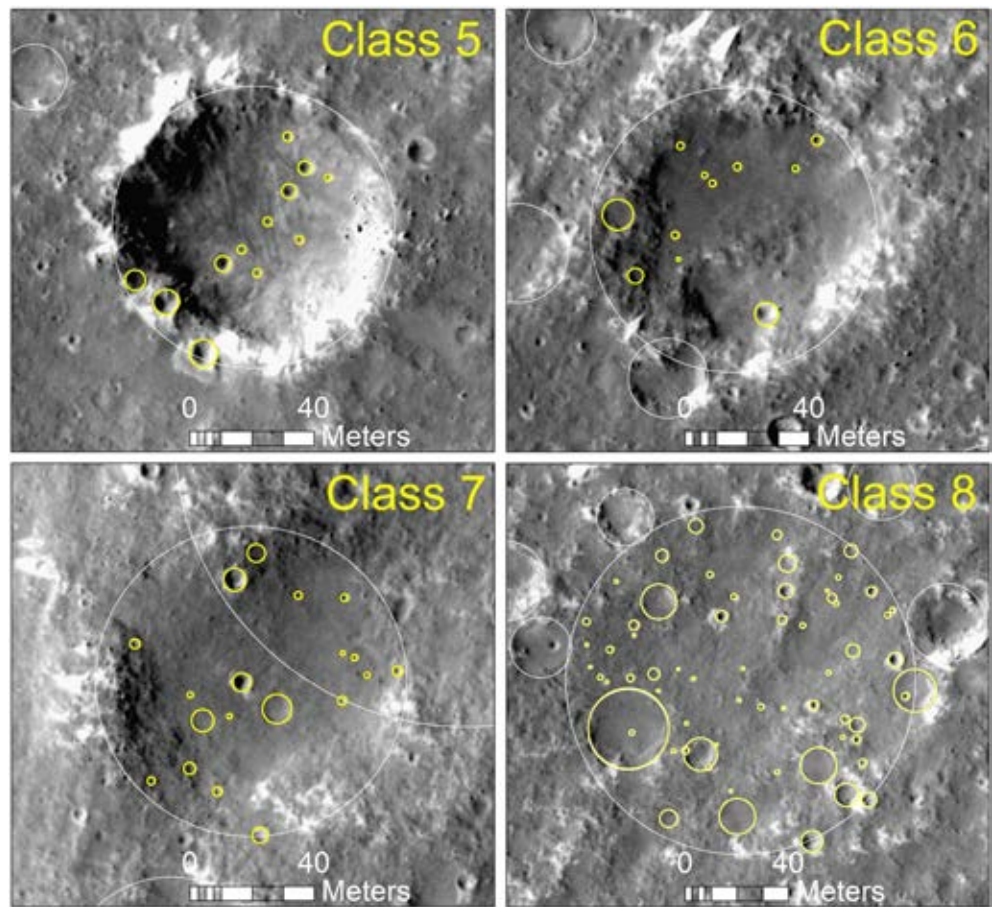


**Figure 8.** Example Classes 5 through 8 craterforms showing superposition of small impact craters on the smooth crater fill materials. The preservation and increasing density of craters on the fill suggests fill stability from Classes 5 through 8. This is consistent with slow, near zero rates of crater filling through this period.

observed superposing the smooth fill. When present, they typically only occur proximal to (and likely are trapped against) the interior of an elevated rim segment. This suggests the possibility that some sand may have migrated across the smooth fill after the fill stabilized. The eolian bedforms currently have a relatively high albedo, likely due to immobility and dust cover (Golombek et al., 2010; Sullivan et al., 2008). All craters between Classes 2 and 6 are identifiable by the presence of bright bedforms. A few dust-covered bedforms have been observed from lander-based images in the vicinity of *Homestead hollow* (Golombek et al., 2020).

Class 7 are the most degraded impact structures in the study region for which an impact origin is unambiguous (Figure 6). They are generally circular (with notable exceptions), flat-floored, are obvious topographic depressions in the HiRISE DEM, and exhibit small, meter-scale remnant elevated rims with gaps exceeding ~50–75% of the circumference of the rim structure. They are distinct from Class 6 by the general lack of large, meter-scale bedforms against the crater rim—a function of near complete rim obliteration (Figure 7). Smaller bedforms may be trapped against the exterior and interior of the remaining rim structures. Class 7 craters also have a generally higher abundance of superposed impact structures (Figure 8), which if large enough, obscure the crater's original planform circularity.

By comparison, the hollows are ambiguous in their origin. They are quasi-circular, flat-floored, sub-meter to meter-deep depressions that typically lack an obvious rim remnant or trapped bedforms. Superposed impact craters are common on their perimeter and floor (Figure 8). We designate the hollows as an eighth morphologic class of circular depression on the landscape. We refer to them throughout the text as “Class 8 hollows” or simply “Class 8” to avoid making the initial assumption that they are genetically related to impact craters.

### 2.3. Crater Morphometry

The morphometric characteristics of all craters in the data set were evaluated using the 1 m HiRISE DEM. Twenty-six of the mapped craters were excluded due to overlap with other craters or overlap with the boundary of the study area. The metrics include crater depth, rim height, rim slope, floor slope, rim curvature (i.e., change in rim slope with distance), floor curvature, ejecta roughness (i.e., standard deviation of elevation), and floor roughness. We hypothesize that all parameters should track with degradation state as expected in the classification scheme. Furthermore, if *Homestead hollow* and other hollow-like features originated as impact craters, their morphometric characteristics should follow a degradation continuum that is consistent with long-term crater obliteration by crater filling and rim degradation.

The morphometric measurements are highly dependent on the vertical precision of the DEM and spatial dimensions over which the parameters are measured. The DEM was produced and edited by the U.S. Geological Survey using the BAE SoftCopy Exploitation ToolSET (SOCET-SET) stereogrammetry program following methods in Kirk et al. (2008). The specific methods for the construction and refinement of the InSight DEMs are outlined in Ferguson et al. (2017) and summarized in Sweeney et al. (2018). The DEMs were subject to a high level of quality control including internal and external evaluation by the U.S. Geological Survey and the Jet Propulsion Laboratory before release for the landing site evaluation. This includes up to 40 hr per DEM of manual inspection and editing to account for blunders or artifacts. The vertical precision of the DEM is  $\sim 0.1$  to  $0.2$  m. This indicates that sub-meter relief should be detectable when measured across the landscape. Figure 9 shows a derived hillshade model that reveals high frequency topographic variations over the smooth intercrater plains that do not correspond with obvious landforms apparent in HiRISE images. We interpret these to be artifacts in the DEM, or “noise.” Here we quantify the influence of DEM noise on the morphometric analysis. We isolated regions of the intercrater plains in the study area and measured the mean and standard deviation ( $\sigma$ ) of relief (difference in elevation), slope ( $^\circ$ ), curvature, and topographic roughness. Each parameter was measured along a 2-m baseline in ArcGIS using a  $3 \times 3$  pixel (i.e., 3 by 3 m) moving window. Five sample areas within the intercrater plains, each at  $\sim 0.01$  km<sup>2</sup>, were selected by cropping the shape of all visible craters and hollows from the DEM, including their continuous ejecta (see Figure 9 for one example sample area). The mean values of relief in the five intercrater regions range from  $0.081$  ( $\sigma = 0.046$  m) to  $0.12$  m ( $\sigma = 0.059$  m), consistent with the minimum DEM vertical precision (Ferguson et al., 2017). Mean slopes range from  $1.76^\circ$  ( $\sigma = 1.03^\circ$ ) to  $2.60^\circ$  ( $\sigma = 1.39^\circ$ ), curvature values from  $-0.17$  m<sup>-1</sup> ( $\sigma = 2.58$  m<sup>-1</sup>) to  $-0.089$  m<sup>-1</sup> ( $\sigma = 3.76$  m<sup>-1</sup>), and roughness values from  $0.026$  m ( $\sigma = 0.014$ ) to  $0.038$  m ( $\sigma = 0.020$  m). These values are used throughout this analysis as a baseline to evaluate whether the craters and hollows are morphometrically distinct from the DEM noise or unique relative to real features that might exist on the intercrater plains. Below, we detail the methodology for measuring the morphometry of the impact craters.

#### 2.3.1. Depth

Crater depth ( $d$ ) is defined here as relief measured from the crest of the crater rim to the deepest portion of the crater floor. To calculate depth, we follow a semi-automated ArcGIS approach, outlined in Sweeney et al. (2018), that allows for the simultaneous measurement of thousands of craters. The circular outline of each crater rim was converted to a series of points, the number of which scales with crater diameter ( $\sim 50$ – $100$  points per crater; Figure 10). Each point was assigned an elevation value from the DEM. A Natural Neighbor interpolation, a form of “area-stealing” interpolation (Sibson, 1981), was used to construct a surface from the 3D points that extends across the crater. Each pixel in the resultant 1-m raster was correlated (or snapped) in  $x,y$  space to the pixel locations of the underlying DEM. Following the interpolation, the DEM was subtracted from the overlying fitted surface to obtain a depth raster (Figure 10a). A maximum crater depth was obtained using Zonal Statistics in ArcGIS, which acquires the maximum depth value from each raster for each individual crater.

Sweeney et al. (2018) tested the semi-automated approach against manual profiling methods. They demonstrated that while this approach provides similar depth values to manual profiling, it benefits by accounting for topographic variability around the entire circumference of the crater rim. However, the results are dependent on the accuracy of the rim digitization, which is difficult to quantify. The results can also be influenced by the presence of large bedforms that are trapped against the rim. Sweeney et al. (2018) reported up to 3 to 5 m of vertical error in the depth measurement for 100-m-scale craters, a result of rim placement uncertainty. For more degraded craters and hollows, placement uncertainty results in sub-meter scale variability in

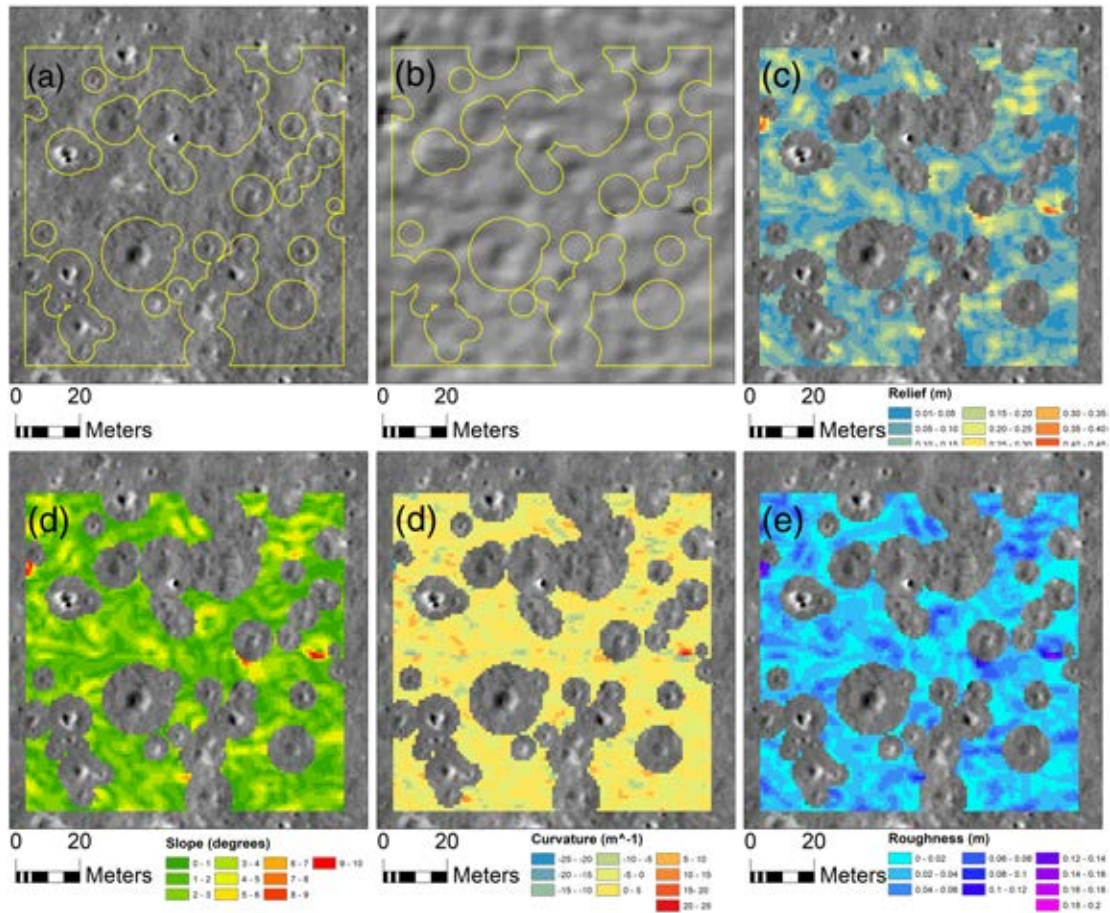


**Figure 9.** Example intercrater region used for the DEM noise analysis. The morphometric characteristics of the intercrater plains were evaluated to make comparisons to the morphometry of the hollows and degraded craters. The intercrater plains represent a baseline on which to evaluate whether the hollow depth, rim height, slope, curvature, and roughness measurements are significant relative to noise in the DEM. (a) A 25 cm per pixel HiRISE image showing the detailed morphology of the smooth, intercrater plains. The lines/border surround the craters and ejecta. Craters and ejecta were excluded from the noise analysis. (b) Hillshade model derived from the 1 m HiRISE DEM. Several topographic features, including small depressions and hills are visible in the hillshade, but are not obvious morphologic features in the image. These are representative of DEM noise. Illumination is from the top left (northwest). (c–f) Relief, slope, curvature, and roughness maps. The values were calculated over a 2-m baseline in ArcMap using a  $3 \times 3$  pixel moving window.

measured depth. The depth of *Homestead hollow* for instance varies from 0.2 to 0.5 m depending on the definition of the rim. While more careful rim digitization methods are possible, three-point rim digitization in CraterTools provides a rapid analysis and compares well against manual profiling results.

### 2.3.2. Rim Height

Rim height ( $h$ ) is defined here as the total relief between the crest of the elevated rim and the surrounding plains at the terminus of the continuous ejecta. Continuous ejecta blankets are not evident in the HiRISE images for most 10-m-scale craters in this area. However, for 100-m-scale RECs, the ejecta blanket extends approximately one crater diameter ( $1D$ ) from the rim crest. Rim height measurements were also acquired using the semi-automated ArcGIS approach by Sweeney et al. (2018). To summarize, a  $1D$  buffer was applied to each crater shapefile. The resultant shapefile represents the total circular area of the crater and its continuous ejecta. The outer edge of this shape was converted to points, and each point was assigned an elevation value from the DEM (Figure 10b). The number of points scales with the area of the ejecta blanket and range from order of 100 points for 10-m-scale craters to order of 1000 points for 100-m-scale craters. A Natural Neighbor interpolation was applied to each crater using the 3D points. The resultant raster represents the approximate elevation and surface slope of the pre-impact surface. To obtain rim height, the underlying interpolated surface was subtracted from the overlying DEM (Figure 10b). Rim digitization uncertainty has a major impact on the rim height measurement. To account for this, the rim height raster was clipped

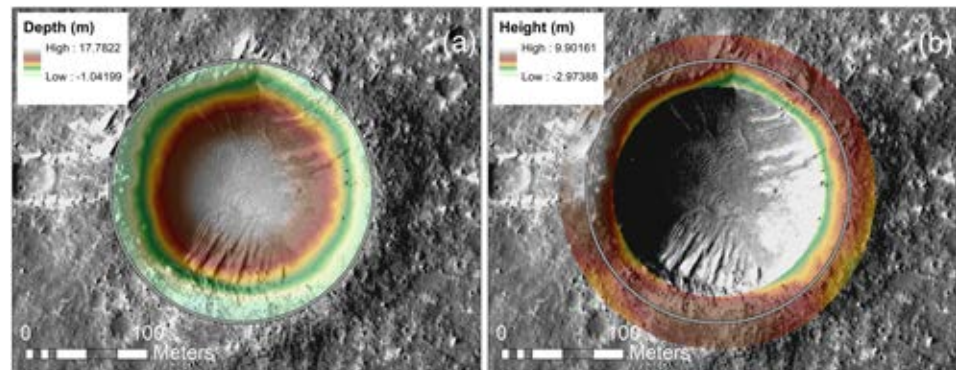


**Figure 10.** (a) Crater depth raster (1 m per pixel). Depth is calculated by fitting a 3D plane across the rim using the points shown. Each point is assigned an elevation value from the HiRISE DEM. The DEM is then subtracted from the overlying 3D surface. (b) Crater rim height raster (1 m per pixel) with the 0.2D annular region that generally defines the majority of the rim structure for all craters. Rim height is calculated by fitting a plane across the continuous ejecta blanket (1D from crater rim). This 3D plane defines the pre-impact surface and is subtracted from the overlying DEM.

by a rim area shapefile, a 0.2D wide annular-shaped area that is centered on the crest of the crater rim. Rim width was found to scale with diameter by  $\sim 0.2D$  (Sweeney et al., 2018). This annular shape generally includes the entire rim structure, incorporating the area between the base of the outer rim slope (at the slope inflection with the continuous ejecta blanket) to the rim interior. The approximate rim width for the smallest 20-m-diameter crater in our analysis is  $\sim 4$  m and is at the threshold of detectability in the hillshade model and DEM. Zonal Statistics were used to extract the maximum and mean rim height from the 0.2D, rim annular shapefile.

### 2.3.3. Rim and Floor Slope

Destruction of a crater rim and filling of the crater interior by local debris and externally derived materials (e.g., eolian sediments) results in a reduction in rim slope and floor slope over time (Craddock et al., 1997; Craddock & Howard, 2000; Forsberg-Taylor et al., 2004; Grant et al., 2006; Armitage et al., 2011; Mangold et al., 2012; Fassett & Thomson, 2014; Watters et al., 2015; Sweeney et al., 2018). Slow, diffusive slope modification and more punctuated events of mass wasting result in rim height degradation, slope reduction, and net transport of material from the rim to the floor (Armitage et al., 2011; Fassett & Thomson, 2014; Sweeney et al., 2018). Impact gardening and eolian processes also operate at the InSight landing site, as evidenced by small superposing craters, nearby hollows, and abundant fines within the hollow (Grant et al., 2020, this issue). Rim height reduction occurs at a rate that nonlinearly decreases with time as slope transport diminishes and the overall landscape becomes weathering-limited (Grant et al., 2006; Sweeney et al. 2018; Grant et al., 2020, this issue). Using a 2D nonlinear topographic diffusion model (see Pelletier & Cline, 2007) Sweeney et al. (2018) demonstrated that slope modification alone could not account for the total observed infilling of craters in the InSight landing ellipse; externally derived materials, such as saltating sand, are required. The resultant filling of the crater should correspond with an overall reduction of floor slope that tracks with increasing crater class.

A slope map, with a 2-m baseline, was constructed using the DEM in ArcGIS for both the rim and floor slope measurements. To calculate the rim slope, the 0.2D annular rim shapefile that represents the entire rim width, was used to clip the slope raster. Maximum and mean slope values were extracted from those areas using Zonal Statistics. Floor slope was calculated using the original circular crater shapefile with the 0.2D annular rim area removed. The resultant floor shapefile includes a portion of the interior crater wall that rests below the average elevation of the surrounding plains. This shape was used with Zonal Statistics to extract floor slope values.

### 2.3.4. Rim and Floor Curvature

Curvature is the measure of the change in slope over distance (Heimsath et al., 1999, 2001). On Earth, hill-slope curvature informs us of the processes that built and modified a landscape which relate to both time, resistance factors (e.g., lithology), climate, and tectonics. More specifically, curvature tracks the overall concavity or convexity of a hill's form and demonstrates regions in a landscape of converging and diverging slopes.

We use curvature here to track the evolution of a crater rim from its initial convex-up form to a more degraded (less convex-up or flat) morphology. Through diffusional hillslope modification processes, the 2D convex-up profile of the rim should be maintained by the steady and spatially uniform removal of materials and filling of the interior. Cratering also subdues the rim, but is a stochastic process. Transport of slope materials from the rim to the crater floor should have the corresponding effect of decreasing the interior concavity of the initial classic crater bowl-shape. Curvature was calculated over a 2-m baseline across a  $3 \times 3$  pixel surface on the DEM. In ArcGIS, a positive value for curvature indicates diverging or convex-up slopes. Conversely, a negative value indicates converging or concave-up slopes. Values close to zero indicate no change in slope and represent either linear slopes or flat surfaces. The 1-m curvature raster was clipped using both the 0.2D annular rim shapefile and the floor shapefile described in the previous section, and was used to calculate maximum and mean values.

### 2.3.5. Floor and Ejecta Roughness

Topographic roughness is defined here as one standard deviation ( $\sigma$ ) of elevation, measured over a 2-m baseline distance. The assumption is that surface processes should result in a decrease in meter-scale roughness of the crater interior (i.e., smoothing of the fill) and destruction of topographic elements in the ejecta blanket over time. Those topographic elements may include 1- to 10-m-scale rocks and 1- to 10-m-scale bedforms. Most rocks and small bedforms are likely below the effective resolution limit of the HIRISE DEM, as is indicated by the analysis of the hillshade model (Figure 9). However, larger features surrounding the largest RECs may be resolved. Standard deviation is calculated using the Focal Statistics tool in ArcGIS. A  $3 \times 3$  pixel rectangular window was used to be consistent with the slope and curvature methods.

## 2.4. Impact Crater Statistics

We provide cumulative (Arvidson et al., 1979) and incremental (Hartmann, 2005) crater frequency plots produced in Craterstats2 (Michael & Neukum, 2010) to evaluate the retention timescales of each crater class and to estimate crater degradation/erosion rates following similar methods to Warner et al. (2010), Golombek et al. (2014), and Sweeney et al. (2018). Crater degradation rates are determined using the time intervals between classes of a specific diameter bin and the changes to crater depth at that same bin. Depth-related degradation is a function of both rim height reduction and crater infilling. It therefore does not provide a true landscape erosion rate. Rim height reduction is used here as a best proxy for landscape erosion. Changes in rim height for each diameter bin are determined between the classes and integrated with the estimated retention ages at the same bin to provide an erosion rate.

For cumulative and incremental plots, we used the Ivanov (2001) and Hartmann and Neukum (2001) production and chronology functions, respectively, to remain consistent with the chronology provided for impact craters measured across the entire landing ellipse in Sweeney et al. (2018). The Hartmann crater equilibrium function (Hartmann, 1984) provided in Craterstats2 is also used. Each plot includes the SFD for all Classes 1 to 8 features, Classes 1 to 7, 1 to 6, and 1 to 5 for the 21-km<sup>2</sup> study area. A cumulative and incremental model age was extracted for each diameter bin from each plot in Craterstats2. The cumulative model age was derived from a fit to the production function for all craters larger than the given bin. The incremental model age was only derived from the craters that populate a bin. The errors reported with each model age refer to counting error, calculated as the square root of  $n$  ( $n$  is the number of craters in that bin), assuming a Poisson sample distribution (Michael & Neukum, 2010). This method does not include a correction for crater widening (see Xie et al., 2017). The total percentage of crater widening over time is highly dependent on target properties, surface processes, and time. Two-dimensional hillslope diffusion models for 100-m-scale craters, applied to craters in the InSight landing ellipse, indicate up to 20% crater widening by Class 5 (Sweeney et al., 2018). Widening has yet to be constrained for 10-m-scale craters or craters more degraded than Class 5 at this location, and an age correction has yet to be defined or applied. Applying a uniform 20% width adjustment to all Class 5 or higher craters accounts for a ~30% decrease in the cumulative model ages on a plot that includes all Class 1 to 8 craters/hollows.

## 3. Results

### 3.1. Crater Mapping and Distribution

Figure 5 provides the crater map color-coded by classification. The total number of craters (including Class 8 hollows) is 2,260. The craters range in diameter from 20 to 272 m. There are 68 craters with diameters

$\geq 100$  m and only six craters in the dataset with diameters  $\geq 200$  m. Of the total number, there are 14 Class 2 craters, 8 Class 3 craters, 26 Class 4 craters, 32 Class 5 craters, 229 Class 6 craters, 636 Class 7 craters, and 1,315 Class 8 hollows. Kernel density maps were produced in ArcGIS to reveal important variations in the spatial distribution of the mapped craters and to evaluate whether the Class 8 hollows have a unique, non-random distribution relative to Classes 1 to 7 craters (Figure 11). Each crater/hollow was assigned a point at their geometric center. The Classes 1 to 8 density map reveals local clusters and dispersed patterns. The density varies by an order of magnitude from  $\sim 50$  to 440 craters per square kilometer. Removing Class 8 hollows from the density calculation however does not eliminate clusters or dispersed patterns. Rather, the Classes 1 to 7 kernel density map also reveals an order of magnitude range in crater density, from  $\sim 20$  to 210 craters per square kilometer, and illustrates a spatial correlation in the clusters and gaps with the Classes 1 to 8 density map. Cratering is a stochastic process (Melosh, 1989). Local clusters and gaps in the cratering pattern are common at the small spatial scale of this analysis, even when secondary crater clusters are ignored (Michael et al., 2012; Warner et al., 2015). We conclude that Class 8 hollows are spatially random and do not have a unique distribution compared to the known craters. In other words, their distribution suggests a similarly stochastic process of formation.

### 3.2. Crater Morphometry

The morphometric data are presented as unbinned and binned  $x,y$  plots with diameter as the independent variable and each morphometric parameter as the dependent variable (see supporting information Data Set S1 for maximum and mean morphometry data; <https://doi.org/10.6084/m9.figshare.11916486.v1>). The plots and statistical analyses use either maximum or mean values. The conclusions drawn from the data do not change with analysis of maximum or mean values. The plots are used, along with a regression analysis, to establish important diameter-dependent scaling relationships and to compare the morphometry of Class 8 hollows to impact craters. We also provide histograms that compare the morphometric data between classes and a principal component analysis (PCA) that considers all eight morphometric parameters in eight-dimensional space. The PCA was performed using the XLSTAT software extension to Microsoft Excel© and the Pearson Correlation coefficient to measure the significance of the association between each morphometric variable. We use the PCA analysis here to explore class-related groupings in the data, to better visualize the Class 8 hollows within a morphologic continuum, and to establish which morphometric variables are more useful for establishing age-related relationships.

#### 3.2.1. Depth

Figures 12a–12c provide unbinned and binned maximum depth ( $d$ ) versus diameter ( $D$ ) plots. Regression statistics (see supporting information Data Set S2 for all regression statistics; <https://doi.org/10.6084/m9.figshare.11916489.v1>) were derived from the unbinned plot. The binned plots are provided for clarity and illustrate the average values of maximum depth for each diameter bin. All data, including the Class 8 hollows, follow a positive linear trend between depth and diameter with coefficients of determination ( $R^2$ ) that decrease from 0.99 for the freshest Class 2 craters to 0.50 for the Class 8 hollows. The probability values ( $p$  values) for the linear fits are all near zero and below the 0.05 alpha threshold (i.e., significance level). Below this threshold there is 95% confidence that a significant statistical relationship exists between depth and diameter.

The trend in the linear fits indicate a similar depth to diameter relationship (within error) of  $d = 0.086D$  and  $d = 0.093D$  for Classes 2 and 3 craters, respectively. From the histogram (Figure 12c), the average depth to diameter ratio ( $d/D$ ) for Classes 2 and 3 craters is lower at 0.059 ( $\sigma = 0.020$ ) and 0.055 ( $\sigma = 0.020$ ), respectively. These classes suffer from low population statistics. Taken together, the functions indicate that the freshest craters in the immediate vicinity of InSight are significantly shallower than typical, pristine simple craters on the Moon and Mars that impacted into competent basaltic rock ( $d = \sim 0.2D$ ) (Daubar et al., 2014; Pike, 1974; Watters et al., 2015). Watters et al. (2015) described similarly shallower depths for impacts into unconsolidated materials, and Sweeney et al. (2018) provided a shallower  $d = 0.15D$  relationship for the freshest craters across the InSight ellipse. From Classes 4 to 8, the linear fits show a decrease in the  $d/D$  relationship from 0.082 to 0.0085, respectively. The observed reduction in the depth to diameter ratio with class follows a predictable, negative trend. From the histogram, the mean of the  $d/D$  values for Class 4 to 8 are 0.056 ( $\sigma = 0.017$ ) for Class 4, 0.044 ( $\sigma = 0.012$ ) for Class 5, 0.029 ( $\sigma = 0.010$ ) for Class 6, 0.020 ( $\sigma = 0.0079$ ) for Class 7, and 0.016 ( $\sigma = 0.0061$ ) for the Class 8 hollows. We conclude that Class 8 hollows have a  $d/D$

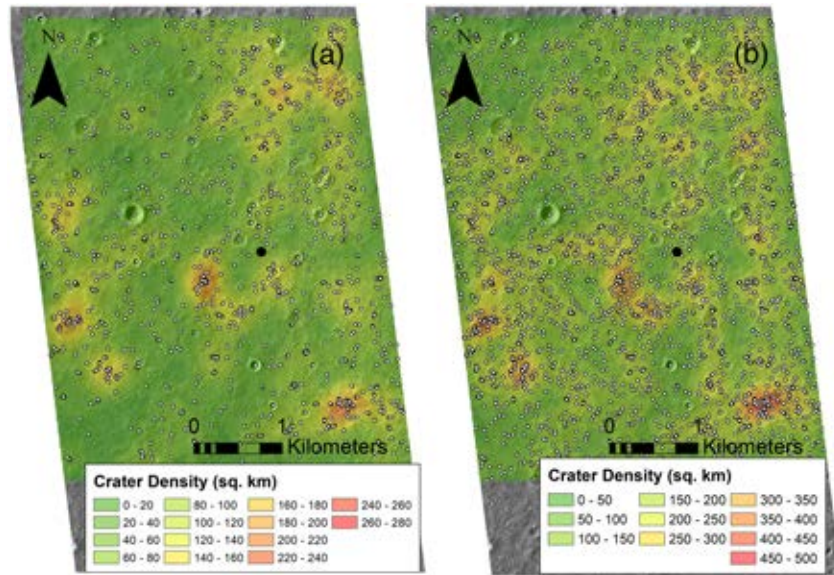


**Figure 11.** (a) Crater density map showing the spatial distribution and number of Classes 1 to 7 craters ( $D \geq 20$  m, each marked by a dot) per square kilometer in the study region. (b) Crater density map showing the spatial distribution and number of Classes 1 to 8 craters/hollows ( $D \geq 20$  m, each marked by a dot) per square kilometer in the study region. The maps indicate that the Class 8 hollows do not have an unusual spatial distribution when compared to known impact craters. Random clusters and dispersed patterns are also evident in the Classes 1 to 7 distribution. The general patterns do not change with inclusion of the hollows. The black dot indicates the location of the InSight lander.

ratio that is consistent with progressive depth-related degradation over time. By definition, all of the hollows have some expression of an enclosed or semi-enclosed topographic depression. The largest and deepest hollow in the study area is 219 m in diameter and 1.8 m deep. By comparison, *Homestead hollow* has a diameter of 27 m and a depth of 0.3 m, or a  $d/D$  ratio of  $\sim 0.011$ , which is well within  $1\sigma$  of the mean in the distribution of all Class 8 hollows. The depth of *Homestead hollow* is just above the threshold of the DEM's vertical precision ( $\pm 0.1$  m - 0.2 m) and relief variation on the intercrater plains ( $\pm \sim 0.08$  m). A fit to the depth and diameter data, including only hollows that are  $\geq 50$  m in diameter, indicate a  $d = 0.0087D$  relationship. For these larger hollows, the error in the vertical precision of the DEMs has less influence. Extrapolating this function down to *Homestead hollow*-size ( $\sim 27$  m diameter) Class 8 features confirms an expected depth of  $\sim 0.2$  m, identical within uncertainty to the measured depth of *Homestead hollow* of  $\sim 0.3$  m.

### 3.2.2. Rim Height

The unbinned and binned maximum rim height ( $h$ ) versus diameter ( $D$ ) plots are displayed in Figures 12d–12f. Maximum rim height is preferred here because it attempts to capture the maximum relief of the crater rim crest within the  $0.2D$  rim annulus relative to the interpolated surface of the surrounding plains. The  $R^2$  values for the linear fits range from 0.97 for the Class 2 data set to 0.39 for the Class 8 hollows. The  $p$  values for the rim height data are also near zero and suggest a significant correlation between rim height and diameter. The fits to both Classes 2 and 3 craters indicate an  $h = 0.048D$  relationship. This is greater than the  $h = 0.036D$  relationship for pristine, simple lunar craters (Pike, 1977) and the  $h = 0.03D$  relationship identified regionally across the InSight ellipse (Sweeney et al., 2018). The mean of the  $h/D$  values from the histogram is more consistent with previously published values and are 0.031 ( $\sigma = 0.014$ ) for Class 2 and 0.032 ( $\sigma = 0.018$ ) for Class 3, although the total number of craters in each of these classes is limited (Figure 12f). Rim height per diameter generally decreases with increasing class. Fits to the Classes 6, 7, and 8 data suggest similar  $h/D$  relationships of  $h = 0.015D$ ,  $h = 0.019D$ , and  $h = 0.014D$ , respectively. However, the mean  $h/D$  values in the histogram for Classes 6, 7, and 8 decrease with increasing class and are 0.025 ( $\sigma = 0.013$ ), 0.018 ( $\sigma = 0.011$ ), and 0.013 ( $\sigma = 0.0098$ ). The Class 8 relationship indicates that the hollows preserve some component of a rim structure, consistent with an impact origin. The largest 100- to 200-m-diameter hollows have 1- to 3-m-tall rims, which is well above the measured relief ( $\pm \sim 0.08$  m) on the smooth intercrater regions.

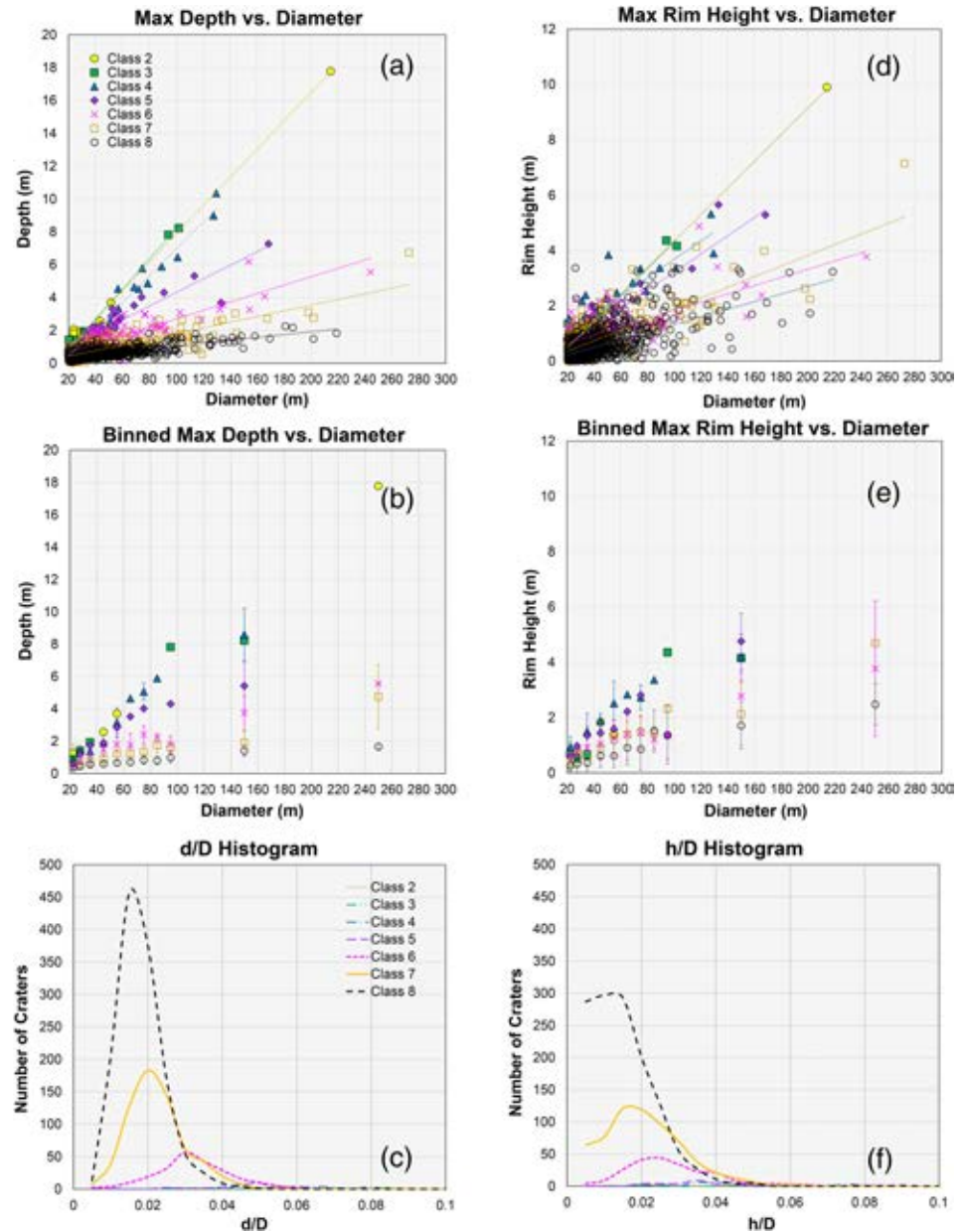


**Figure 12.** Crater morphometric data for maximum depth and rim height. (a) Unbinned maximum depth ( $d$ ) versus diameter ( $D$ ) plot showing Classes 1 to 8 craters. (b) Binned maximum  $d$  versus  $D$  plot. Each bin represents the mean of the maximum depth values. The error bars represent one standard deviation around the mean. (c) Histogram showing the distribution of  $d/D$  values for Classes 6, 7, and 8. Lower classes not visible due to poor sample statistics. (d) Unbinned maximum rim height ( $h$ ) versus  $D$  plot showing class 1 to 8 craters. (e) Binned maximum  $h$  versus  $D$  plot. Each bin represents the mean of the maximum rim height values. The error bars represent one standard deviation around the mean. (f) Histogram showing the distribution of  $h/D$  values for Classes 6, 7, and 8. Lower classes not visible due to poor sample statistics. The data confirm that the Class 8 hollows fall along the degradational continuum of impact craters in the landing site. They are only slightly more degraded relative to Classes 6 and 7 samples.

The unbinned maximum rim height plot and  $h/D$  histogram illustrate significant scatter in the data when compared to the depth and diameter relationship. Similar scatter was identified in the Sweeney et al. (2018) data set and was described by Watters et al. (2015) in their analysis of simple Martian craters. Geologic explanations for this scatter include: (1) variability in the height of the initial rim structure after impact and (2) non-uniform degradation of the rim structure over time. Sweeney et al. (2018)



demonstrated significant topographic variation in the maximum rim height of fresh (Classes 1 and 2), 10- to 100-m-scale craters in the InSight landing ellipse. This suggests that the most proximal ejecta may be emplaced non-uniformly, possibly due to irregularity in the initial topography of the target site, differences in target strength (rock vs. regolith), or impact trajectory. Furthermore, their analysis of more-degraded craters in the region indicated that topographic variation in the rim is preserved throughout degradation. The new analysis confirms that gaps and peaks exist in the rim structure of even extremely degraded craters.

Other explanations for the rim height variance are related to the method of calculation. Rim height can be over or underestimated depending on the topographic features that intersect the interpolated raster of the surrounding plains. Other craters that intersect this plain will cause a local low to form in the raster and will lead to an overestimate in the maximum rim height. Positive topographic features, such as other crater rims, will create local highs in the raster. In the case of Class 8 *Homestead hollow*-size features, the rim height values straddle zero, but can be as high as 1.2 m. *Homestead hollow* itself has a measured, maximum rim height using this method of  $\sim 0.2$  m (along southeast rim segment). In this case, the southeast sloping terrain and minor topographic variations on the plains immediately surrounding the hollow result in this maximum rim height estimate. Manual measurements on the DEM, acquired from the northern and western margins of *Homestead hollow* confirm a 0 to 0.2-m rim height. Taken as a group, *Homestead hollow*-size features have a mean rim height of  $\sim 0.3$  m ( $\sigma = 0.3$ ), which is just above the vertical precision and noise in the DEM. Bedforms can also complicate the rim height calculation for the more pristine craters and may explain their unusually large maximum height versus diameter relationship.

### 3.2.3. Rim and Floor Slope

Figures 13a–13c present the maximum and mean slope data for crater rims and floors. The binned plot indicates that the average of the maximum rim slope generally decreases with increasing class, consistent with rim degradation through time. The unbinned data however reveal significant variation around the mean for all crater classes and at all size bins. Classes 2, 3, and 4 rim structures hold maximum slopes of  $\sim 30^\circ$  to  $40^\circ$ , which is at or just slightly above the angle of repose for loose sand, granules, and pebbles. HiRISE images and the DEM confirm that the steepest slopes on the rims of the freshest craters correspond with either exposed meter-size rocks in the larger, 100-m-scale impact craters (rocks ejected from depth), or meter-scale eolian bedforms. As the craters degrade through Classes 5 to 7, the maximum slopes generally decrease, but a broad range of values exist, spanning  $4^\circ$  to  $30^\circ$ . Class 8 hollows, including *Homestead hollow* ( $\sim 8^\circ$ ), also show a similar range in maximum slopes but tend to be most similar to, if not more degraded than, the Class 7 variety. In all cases, a  $\pm 2^\circ$  error due to DEM noise, indicated in the hillshade model and slope analysis of the intercrater plains, should be considered.

The variation in the slope in each class is indicative of the complexity of rim morphology and is likely related to overlapping impact craters, bedforms, erosional exposure of large blocks, and depth-related variations in target properties. The data also indicate a positive linear relationship between maximum rim slope and diameter. The  $R^2$  values are fairly low, and the standard errors are relatively high indicating significant variation around the fit. All  $p$  values are higher relative to the depth and rim height plots, but still fall below the 0.05 threshold. Using the binned plot, the average maximum slope values in each diameter bin of Classes 2 through 4 craters generally increase from  $\sim 15^\circ$  to  $\sim 35^\circ$  as the crater diameter increases from 20 to 100 m. More degraded craters inherit the relationship of increasing slope with increasing diameter. Class 8 hollows generally hold a  $\sim 7^\circ$  maximum rim slope at the 20-m-diameter bin and a  $\sim 14^\circ$  maximum rim slope at the 100-m bin. Figure 13c provides the histogram for maximum slope versus diameter. A possible explanation for the slope increase is related to the total width of the crater rim relative to the pixel distance over which the slopes are calculated. For 20 m diameter craters, the  $0.2D$  rim annulus is only 4 m wide. The steepest portion of the rim for craters of this size may be less than the scale of the slope measurement (2-m baseline). However, the maximum slope steadily increases even for larger craters where the steepest portion of the rim encompasses dozens of pixels. An increase in rim slope with diameter was also found by Sweeney et al. (2018) and was attributed to changes in regolith characteristics with depth. From observations of concentric craters and RECs in the landing ellipse, Warner et al. (2017) determined that a strength transition occurs at  $\sim 2$ - to 5-m

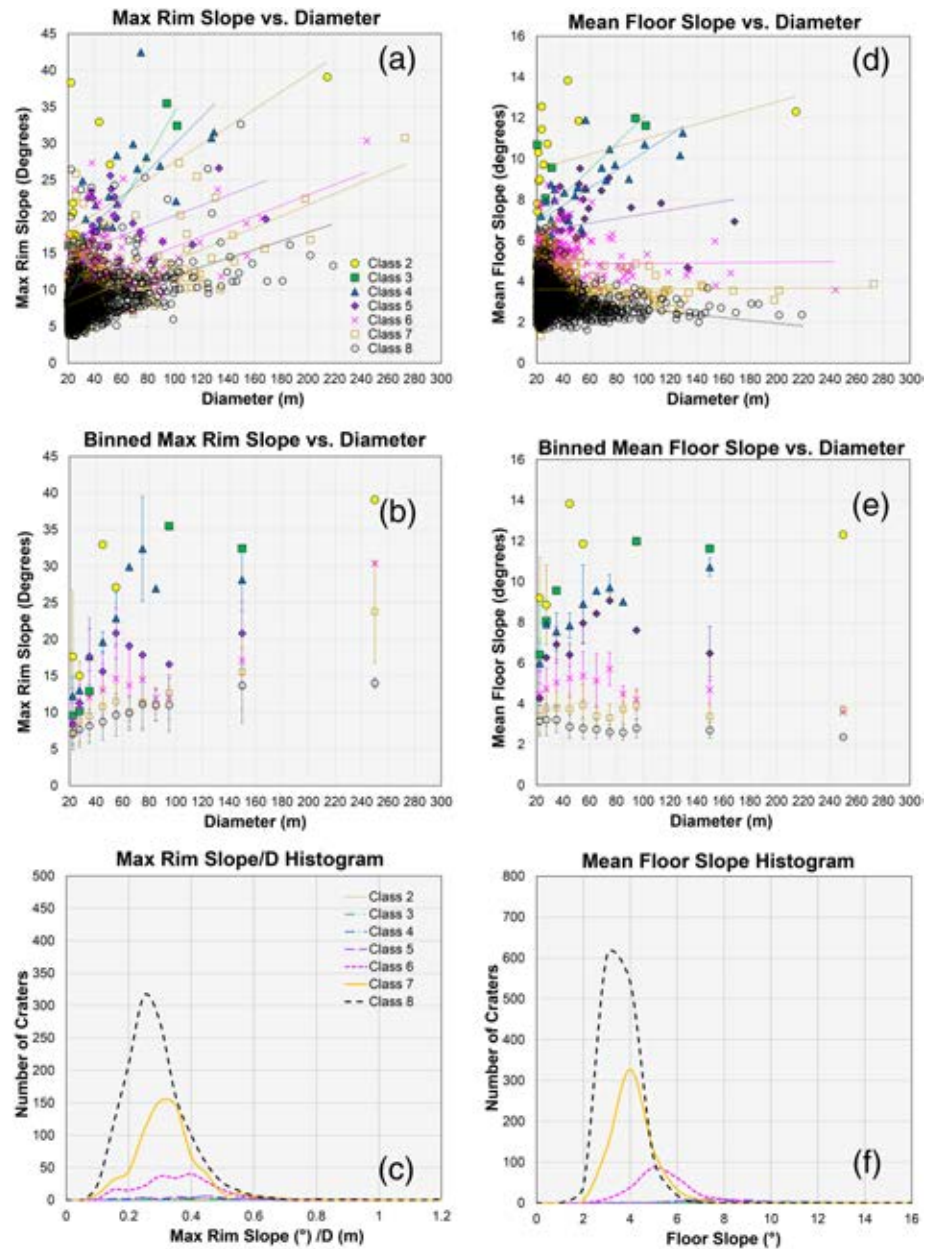


**Figure 13.** Crater morphometric data for maximum rim slope and mean floor slope. (a) Unbinned maximum rim slope ( $^{\circ}$ ) versus diameter ( $D$ ) plot showing Classes 1 to 8 craters. (b) Binned maximum rim slope versus  $D$  plot. Each bin represents the mean of the maximum rim slope values. The error bars represent one standard deviation around the mean. (c) Histogram showing the distribution of maximum rim slope normalized to  $D$  for every crater in Classes 6, 7, and 8. Lower classes not visible due to poor sample statistics. (d) Unbinned mean floor slope ( $^{\circ}$ ) versus  $D$  plot showing Classes 1 to 8 craters. There is no statistical relationship between floor slope and crater diameter. (e) Binned mean floor slope (non-normalized) versus  $D$  plot. Each bin represents the average of the mean rim height values. The error bars represent one standard deviation around the mean. (f) Histogram showing the distribution of mean floor slope values for Classes 6, 7, and 8. Lower classes not visible due to poor sample statistics. The data confirm that the Class 8 hollows fall along the degradational continuum of impact craters in the landing site. They are only slightly more degraded relative to Classes 6 and 7 samples.

depth. At this depth and beyond, meter-size rocks are excavated by larger, >100-m-scale craters. Shallower than this depth, meter-size rocks are generally absent or very limited in abundance. The presence of rockier materials in the proximal ejecta of larger, 100-m-scale craters might explain the steeper slopes and overall resistance to degradation.

Floor slope data reveal a similar decrease with increasing class (Figures 13d–13f). HiRISE observations indicate a transition in floor morphology with time from eolian bedforms that hold slopes close to the angle of repose to smooth surfaces that lack appreciable relief. Here we present the mean floor slope data. The mean is preferred in this case due to the abundance of small, superposed impact craters on the smooth infill of the most-degraded examples. These craters generate slopes that mimic the bedforms in the fresher classes. A mean slope value represents the average of all pixels queried by Zonal Statistics within the shapefile that defines the crater floor.

Unlike depth, rim height, and rim slope, there is no significant correlation between mean floor slope and diameter. The  $p$  values are close to or significantly greater than 0.05. All  $R^2$  values are also generally low, ranging from 0.57 for the Class 4 fit down to 0.0001 for Class 7. While there is scatter in the data set, and significant overlap between classes, the higher classes generally have a lower mean floor slope than the freshest craters. From the binned plot, Classes 2 and 3 craters hold average floor slopes between  $7^\circ$  and  $14^\circ$ . From the histogram, the mean of the average floor slopes of the freshest two classes are  $9.9^\circ$  ( $\sigma = 2.3$ ) for Class 2 and  $8.3^\circ$  ( $\sigma = 1.5$ ) for Class 3 (Figure 13f). Maximum floor slopes in those same classes approach  $40^\circ$ , consistent with the presence of eolian bedforms. The interior fill of Class 4 and older craters is characterized by a relatively smooth and planar surface with mean floor slopes ranging from  $\sim 2^\circ$  to  $10^\circ$ . The interiors of Class 8 hollows, including *Homestead hollow*, are only slightly smoother than Class 7 impact craters. From the binned plot, the mean floor slope of Class 7 craters in each diameter bin is between  $3^\circ$  and  $5^\circ$  while the hollows range from  $2^\circ$  to  $4^\circ$ . From the histogram, the mean of the average floor slope values for Class 8 hollows is  $3.1^\circ$  ( $\sigma = 0.7$ ), which is only slightly rougher than the smoothest terrains on the intercrater plains ( $\sim 2^\circ$ ). The floor of *Homestead hollow* has an identical mean floor slope of  $3.1^\circ$ . By comparison, the Classes 6 and 7 mean average floor slope values are  $4.8^\circ$  ( $\sigma = 1.1$ ) and  $3.6^\circ$  ( $\sigma = 0.8$ ), respectively.

#### 3.2.4. Rim and Floor Curvature

Mean rim curvature and mean floor curvature are presented here to establish the overall, average hillslope form of the craters and hollows (Figures 14a–14f). The mean rim curvature values for all craters are mostly positive, consistent with an overall convex up hillslope morphology. The data also suggest that there is a weak statistical relationship between rim curvature and diameter. The regression analysis indicates a range of weakly negative to nearly flat linear relationships between these two parameters. The fits provide very low  $R^2$  values that range from a maximum of 0.347 for Class 2 to a minimum of 0.0019 for Class 3. However, the  $p$  values for Classes 2, 5, 6, 7, and 8 are all below the 0.05 confidence threshold. The curvature data indicate that steeper, likely rock-bearing slopes in larger craters hold a more linear hillslope form (near zero curvature). We suggest that the interior rim slopes of larger, (order of) 100-m-diameter craters that contain rockier materials differentially weather largely by mass wasting processes that include a combination of granular creep from overlying regolith and rock falls/rolls from the blockier ejecta. Similar to weathering-limited terrestrial hillslopes, these rockier slopes can retain a more angular/linear form. In contrast, entirely granular rims degrade by a combination of slow diffusive creep and granular flows in a manner similar to terrestrial, soil-mantled hillslopes (Heimsath et al., 1999). These slopes trend towards a more parabolic form with a measureable curvature.

The data also indicate a constant reduction in the curvature of the rim with increasing class, including Class 8 hollows. From the histogram, normalizing curvature for variations with diameter, the average curvature/ $D$  values for Classes 2 to 5 are 0.10 ( $\sigma = 0.047$ ), 0.065 ( $\sigma = 0.044$ ), 0.052 ( $\sigma = 0.029$ ), and  $0.039 \text{ m}^{-2}$  ( $\sigma = 0.025$ ), respectively (Figure 14c). By comparison, the Classes 6, 7, and 8 average values are 0.032 ( $\sigma = 0.025$ ), 0.013 ( $\sigma = 0.019$ ), and  $0.0050 \text{ m}^{-2}$  ( $\sigma = 0.014$ ). The average rim curvature/ $D$  value for *Homestead hollow* is more similar to the Class 7 variety at  $0.010 \text{ m}^{-2}$ . The reduction in curvature, but maintenance of the convex form (i.e., positive curvature values), suggests the importance of diffusional hillslope modification processes (Heimsath et al., 1999, 2001; Pelletier & Cline, 2007; Fassett & Thomson, 2014; Sweeney et al., 2018). Only the more degraded Classes 6 through 8 examples provide a lower end of negative curvature values that are consistent with the average curvature of the intercrater plains.

Mean floor curvature values are all generally negative for all classes indicating a concave-up morphology that is consistent with a bowl-shaped interior form (Figures 14d–14f). The morphologically more-pristine classes exhibit increasingly lower (more negative) interior curvature values relative to the more degraded classes, which is indicative of progressive filling and flattening of the bowl-shape. The binned and

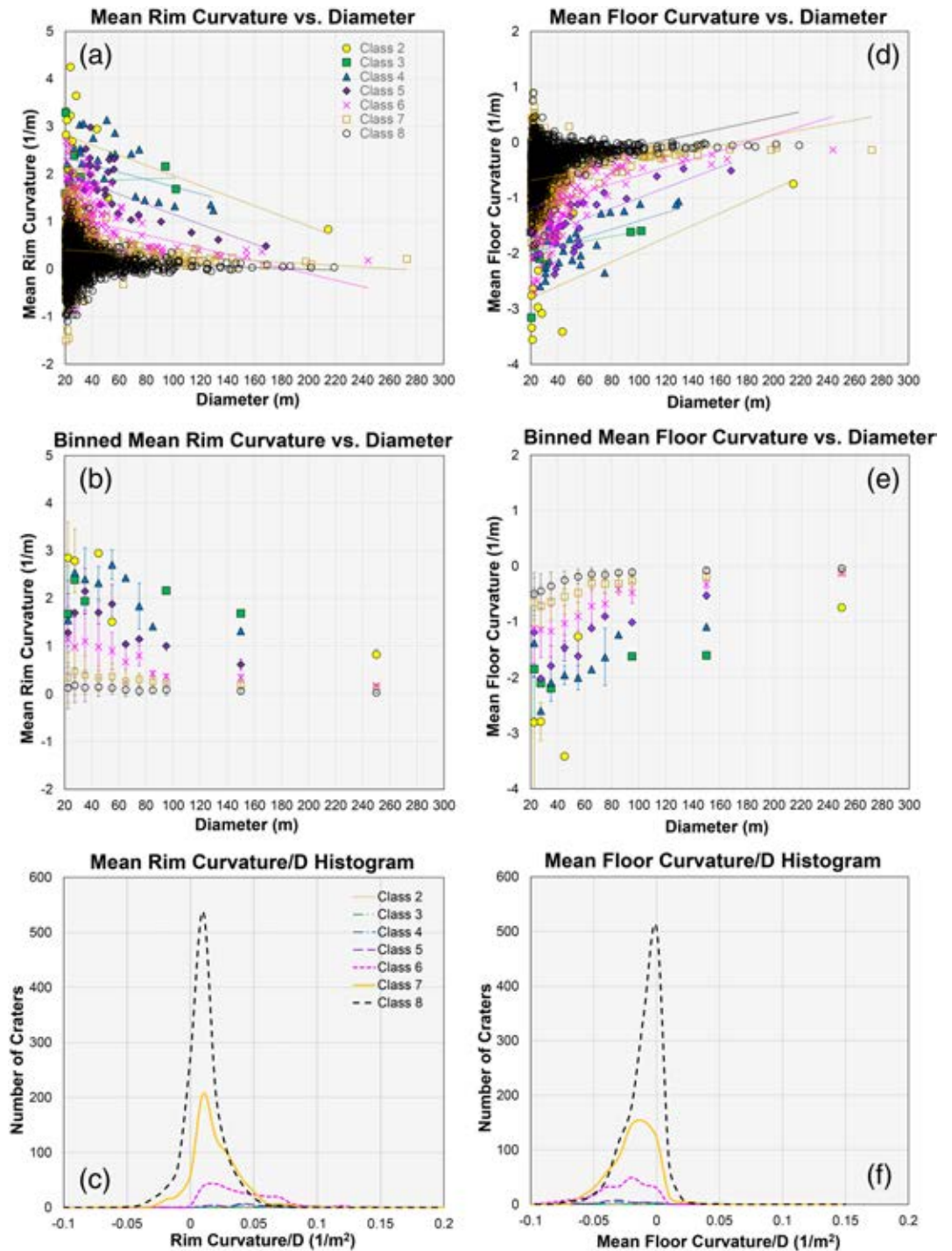


**Figure 14.** Crater morphometric data for mean rim and floor curvature. (a) Unbinned mean rim curvature versus diameter ( $D$ ) plot showing Classes 1 to 8 craters. (b) Binned mean rim curvature versus  $D$  plot. Each bin represents the average of the mean rim curvature values. The error bars represent one standard deviation around the mean. (c) Histogram showing the distribution of mean rim curvature/ $D$  values for Classes 6, 7, and 8. Lower classes not visible due to poor sample statistics. (d) Unbinned mean floor curvature versus  $D$  plot showing Classes 1 to 8 craters. (e) Binned mean floor curvature versus  $D$  plot. Each bin represents the average of the mean floor curvature values. The error bars represent one standard deviation around the mean. (f) Histogram showing the distribution of mean floor curvature/ $D$  values for Classes 6, 7, and 8. Lower classes not visible due to poor sample statistics. The data confirm that the Class 8 hollows fall along the degradational continuum of impact craters in the landing site. They are only slightly more degraded relative to Classes 6 and 7 samples.

unbinned plots reveal that the interiors of Class 8 hollows have a near zero, but still mostly negative average floor curvature. The floor curvature of *Homestead hollow* for instance is  $-0.42 \text{ m}^{-1}$ . Class 8 hollows are similar in form to Class 7 impact craters.

The data also reveal a very weak positive relationship between mean floor curvature and diameter. The  $R^2$  values are extremely low and range from 0.047 for Class 4 to 0.30 for Class 5 craters. The  $p$  values obtained from the linear regression show a statistically significant positive relationship for some classes and no relationship for others. The crater floor area does not include the rim structure, but does include portions of the interior crater wall that exists below the average elevation of the surrounding plains. The positive scaling relationship may also be related to variations in material properties exposed in the walls of small and large craters, although a similar relationship is not seen between diameter and maximum interior floor slope. Additionally, bedforms and superposed impact structures influence interior crater morphology. For the younger impact craters, bedforms scale with the size of the crater and may create locally large convex landforms (e.g., ripples and dunes) that bias the mean curvature calculation to more positive values.

### 3.2.5. Ejecta and Floor Roughness

The mean floor roughness data exhibit a general increase in topographic roughness for fresher impact craters (Figures 15a–15c). This suggests the importance of bedforms and the preservation of topographic relief on the interior crater wall in younger craters. All roughness values for Classes 2 to 7 craters exceed the roughness of the smooth intercrater plains ( $\sim 0.03 \text{ m}$ ). From the histogram, the average of the mean floor roughness values range from 0.14 m ( $\sigma = 0.036 \text{ m}$ ) for Class 2 craters to 0.053 m ( $\sigma = 0.012 \text{ m}$ ) for Class 7 craters. Class 8 hollows by comparison also have a slightly higher mean floor roughness value when compared to the smooth plains at 0.046 m ( $\sigma = 0.010 \text{ m}$ ). By comparison, *Homestead hollow* has an identical mean floor roughness value to the average for all Class 8 of 0.046 m. The regression analysis further indicates that there is no relationship between floor roughness and crater diameter. The  $p$  values for each crater class are consistently above the 0.05 threshold, and the  $R^2$  values suggest significant variation around the fits.

Unlike all other parameters evaluated here, there is no apparent relationship between roughness in the ejecta and class (Figures 15d–15f). There is also no correlation with crater diameter. From the histogram, the average of the ejecta roughness values ranges between 0.036 m ( $\sigma = 0.0060 \text{ m}$ ) for Class 8 hollows and 0.045 m ( $\sigma = 0.017 \text{ m}$ ) for Class 2 craters. Both of these values are similar to the average topographic roughness measured on the smoothest intercrater plains (Figure 9). This suggests that none of the craters in the 21-km<sup>2</sup> region surrounding the InSight lander have excavated rocks that are large enough to be detected by the HiRISE DEM. Figure 16 highlights a 102-m-diameter Class 3 rocky ejecta crater. Meter-size rocks are apparent in the HiRISE image, but they are insufficient in vertical and horizontal scale to be resolved in the DEM.

### 3.2.6. Principal Component Analysis

The results of the PCA are displayed in Figures 17 and 18. The morphometric variables that have a statistically significant diameter dependence were normalized to diameter. The outputs of the XLSTAT program include biplots and correlation circles. The biplot combines a standard PCA plot with a correlation circle. A PCA reduces and simplifies the dimensions of multivariate data (in this case eight morphometric variables) by transforming the data onto a two dimensional,  $x,y$  plot that is defined by two principal components. The first principal component (F1) defines the  $x$  direction of the linear transformation (or eigenvector) and accounts for the bulk of the variance in the data. Each subsequent component is orthogonal to the preceding component (F2 is orthogonal to F1) and captures additional variance in the data. The correlation circles provide vectors for the active variables (the morphometric parameters) in  $x,y$  principal component space and indicate which variables are most closely correlated. Low angles between the vectors indicate a significant positive correlation, orthogonal angles indicate no relationship, and obtuse angles suggest a negative correlation. A larger vector magnitude that is distal to the center of the circle indicates that the given principal components capture the bulk of the variability in the data. However, if the vector ends close to center, other components carry some of the information. We present the data for Classes 1 to 8 craters and hollows (Figure 17) as well as only Classes 1 to 7 craters (Figure 18).

The Classes 1 to 8 correlation circle for the first (F1) and second (F2) principal components captures  $\sim 69\%$  of the total variability in the data (Figure 17a). We also present the first (F1) and third (F3) components which capture  $\sim 67\%$  of the information (Figure 17b). The results indicate that the most strongly, positively

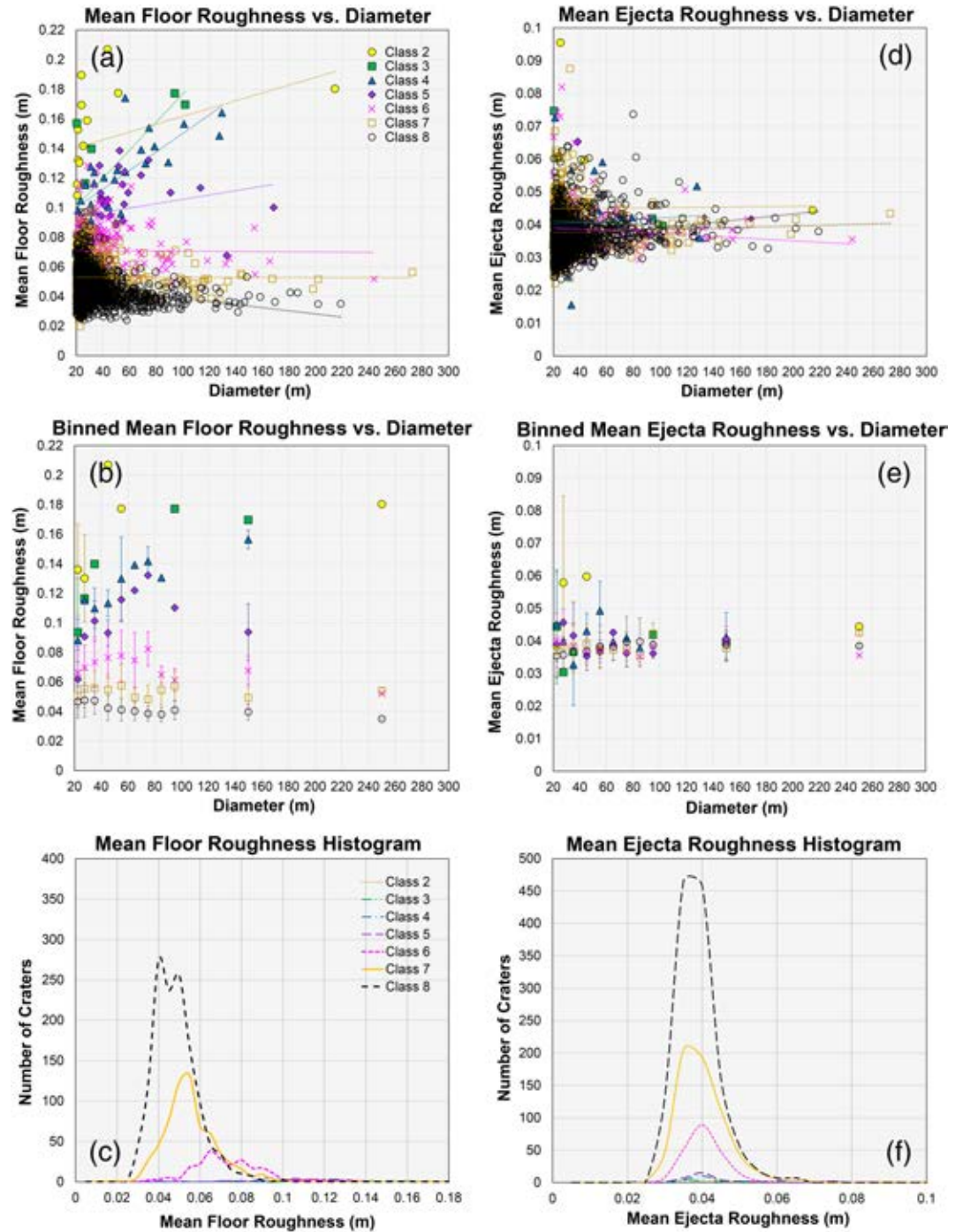


**Figure 15.** Crater morphometric data for mean floor and ejecta roughness. (a) Unbinned mean floor roughness versus diameter ( $D$ ) plot showing Classes 1 to 8 craterforms. (b) Binned mean floor roughness versus  $D$  plot. Each bin represents the average of the mean floor roughness values. The error bars represent one standard deviation around the mean. (c) Histogram showing the distribution of mean floor roughness values for Classes 6, 7, and 8. Lower classes not visible due to poor sample statistics. (d) Unbinned mean ejecta roughness versus  $D$  plot showing Classes 1 to 8 craterforms. (e) Binned mean ejecta roughness versus  $D$  plot. Each bin represents the average of the mean ejecta roughness values. The error bars represent one standard deviation around the mean. (f) Histogram showing the distribution of mean ejecta roughness values for Classes 6, 7, and 8. Lower classes not visible due to poor sample statistics. The data confirm that the Class 8 hollows fall along the degradational continuum of impact craters in the landing site. They are only slightly more degraded relative to Classes 6 and 7 samples. However, there is no relationship between ejecta roughness and class.

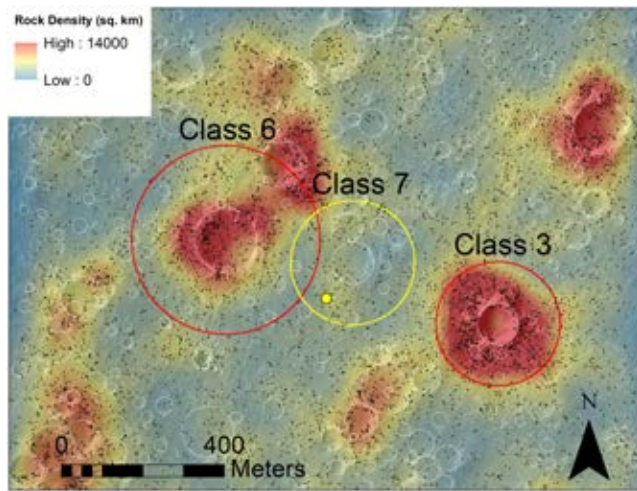


**Figure 16.** Rock density map showing the location of manually digitized rocks (visible at HiRISE resolution) and the continuous ejecta blankets (assuming  $1D$  distance from crater rim) of rocky ejecta craters that are proximal to InSight (yellow filled dot). The crater statistics indicate that *Homestead hollow* is older than the Class 3 crater to the southeast and is possibly older than the Class 6 crater to the northwest. The rock density map does not indicate an unusually high rock abundance resulting from ejecta from either of these craters, although *Homestead hollow* may be in range of the discontinuous ejecta of the Class 6 crater. This is a possible source for *Rocky Field* (Grant et al., 2020, this issue). The crater data indicate that *Homestead hollow* postdates the 102-m-diameter Class 7 crater northeast of the landing site. *Homestead hollow* rests within range of the continuous ejecta of this crater.

correlated morphometric variables in this analysis are mean floor roughness, mean floor slope, and  $d/D$ . Mean floor curvature/ $D$  is also strongly negatively correlated with these parameters. The bulk of the variance in the data occurs along the first principal component. Maximum  $h/D$ , maximum rim slope/ $D$ , and mean rim curvature/ $D$  are all weakly correlated with each other and with the floor-related parameters. They also carry information in both the second and third components. Mean ejecta roughness is an outlier and is not correlated with the other parameters.

The Classes 1 to 8 biplots illustrate how the individual craters plot in principal component space (Figures 17c and 17d). The correlation circles are superposed for comparison. The bulk of the data cluster near the origin on both the F1/F2 and F1/F3 biplots. The cluster corresponds with the Classes 7 and 8 varieties, with Class 8 hollows having generally lower values for all morphometric parameters (aside from mean floor curvature). Fresher craters plot as clear endmembers in principal component space. The data cloud extends along the first principal component axis in the vector direction of the  $d/D$ , mean floor slope, and mean floor roughness, indicating that these variables are the most representative of the morphometric variation between the different classes. While the values for Class 2 craters tend to be highest, there is significant overlap with Classes 3 and 4 craters.

Figures 18a–18d provide the correlation circles and biplots for the data set with Class 8 hollows removed. Despite the overwhelmingly large number of Class 8 hollows in the data set, removing them from the multivariate analysis does not change the PCA results. This suggests that the morphometry of the hollows, considering all eight parameters, is consistent with an impact origin. Furthermore, we conclude that crater depth, and the

other interior morphometric parameters, are the best predictors of the relative age of craters on this landscape. Rim-related variables are not only weakly correlated with each other and the crater interior morphology, but are less representative of the classification scheme. This is likely a result of the aforementioned complexity in crater rim morphology, stratigraphy, degradation, and rim identification.

In summary, the spatial distribution and morphometry of the Class 8 hollows indicate that they are part of a continuum of crater rim degradation and infilling. Class 8 hollows are only slightly more-degraded than Class 7 impact craters and yet are morphologically distinct topographic depressions (some with elevated rims) by comparison to the intercrater plains. We therefore conclude that Class 8 hollows, and by extension *Homestead hollow*, are degraded impact craters.

#### 4. Crater Retention Ages & Erosion Rates

Figure 19 provides cumulative and incremental crater size-frequency plots for Classes 1 to 5, 1 to 6, 1 to 7, and 1 to 8 craters. Consistent with the morphometric analysis, the SFD of the Class 8 hollows points to an impact origin. The distribution for all  $D \geq 100$ -m-scale craters, including the hollows, follows a  $-3.2$  power law slope that is similar to the crater production function (Ivanov, 2001). The  $D \leq 100$ -m-scale population generally follows a  $-2$  slope that is similar to the crater equilibrium function (Hartmann, 1984). This equilibrium condition points to slow, steady state destructive processes, where craters are produced at a similar rate to their obliteration. This is opposed to more punctuated obliteration mechanisms that more efficiently resurface all craters below a specific diameter threshold (e.g., lava flow burial and fluvial erosion). Model ages derived from the  $D \leq 100$  m population (Table 1) are representative of the ability of the landscape to retain craters over specific exposure timescales.

The cumulative and incremental plotting methods both indicate Early to Late Amazonian retention ages for 10-m-scale craters (Michael, 2013 epoch boundaries) (Table 1). Classes 7, 6, and 5 craters of *Homestead hollow*-size have Late Amazonian, cumulative-derived retention ages of  $300 \pm 10$ ,  $140 \pm 10$ , and  $50 \pm 7$  Myr, respectively. The incremental ages for Classes 7 to 5 craters are generally younger at  $170 \pm 6$ ,

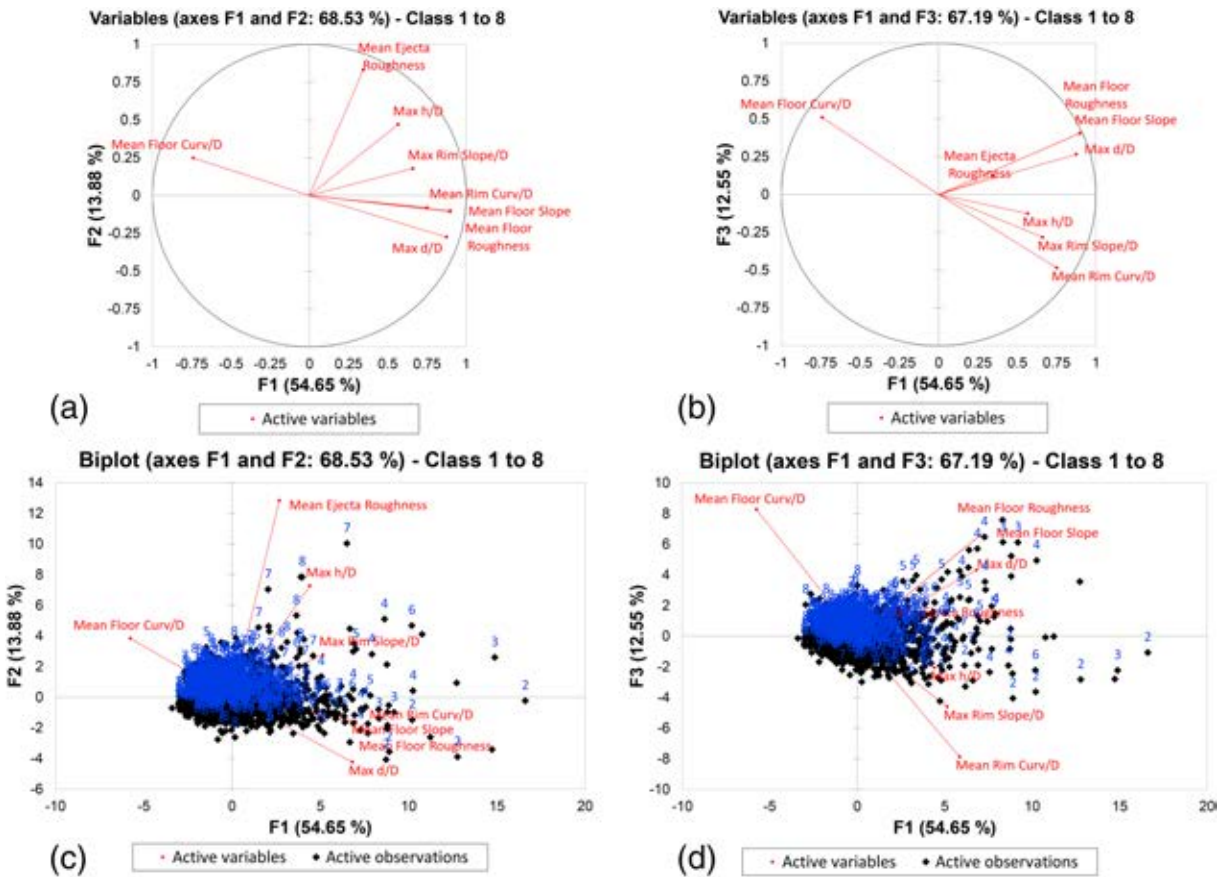


**Figure 17.** Results of the principal component analysis for all eight morphometric parameters for Classes 1 to 8 craterforms. (a) Correlation diagram showing components F1 and F2. The correlation circles provide vectors for the active variables (the morphometric parameters) in  $x,y$  principal component space and indicate which morphometric variables are most closely correlated. Low angles between the vectors indicate a significant positive correlation, orthogonal angles indicate no relationship, and obtuse angles suggest a negative correlation. A vector magnitude that is distal to the center of the circle indicates that the given principal components capture the bulk of the variability in the data. (b) Correlation diagram showing F1 and F3. Mean floor slope, mean floor roughness, and  $d/D$  are the most strongly correlated on both plots and are better predictors/representatives of the overall morphometric classification scheme. (c and d) Biplots showing the distribution of the crater data plotted in principal component space (black plus symbols). The freshest craters (Classes 2, 3, and 4) are obvious end members, plotting along the first principal component axis (F1). The more degraded craters are clustered near the origin. Each data point is labeled with the crater class (blue numbers).

$55 \pm 3$ , and  $15 \pm 2$  Myr. The cumulative and incremental frequencies of Class 8, *Homestead hollow*-size ( $\sim 27$  m in diameter) features provide Middle Amazonian model ages of  $680 \pm 20$  ( $D \geq 25$ -m bin) and  $400 \pm 9$  Myr (22.1- to 31.2-m-diameter bin), respectively. One-hundred-meter-scale Class 8 hollows indicate a maximum Early Amazonian model age, derived from the cumulative frequency histogram of Classes 1 to 8 craters, of  $1.8 \pm 0.2$  Gyr. The age derived from the incremental frequency above 100 m confirms a similar model age (Table 1). By comparison, the model age determined using the cumulative frequency of all craters larger than 200 m across the entire InSight landing ellipse is similar at  $1.7 \pm 0.1$  Gyr (Warner et al., 2017). Previous geologic mapping and impact crater statistics revealed an Early Hesperian age for the ridged lava plains at the landing site (Tanaka et al., 2014), but the statistics in that mapping effort were derived from craters with diameters  $>5$  km. Warner et al. (2017) confirmed an Early Hesperian model age of  $\sim 3.6$  Gyr using craters  $>2$  km in diameter. The InSight landing site therefore records three distinct crater populations: (1) a population of 10-m-scale craters that are at equilibrium with Early to Late Amazonian-age surface processes, (2) an Early Amazonian population of 100-m-scale craters that follow a production distribution (Warner et al., 2017 and this study), and (3) a kilometer-size population that records a maximum Early Hesperian production age. Regional mineralogic, stratigraphic, and geologic relationships, including spectral observations of mafic minerals in fresh craters and the identification of infilled, ancient kilometer-size craters (e.g., ghost craters) suggest



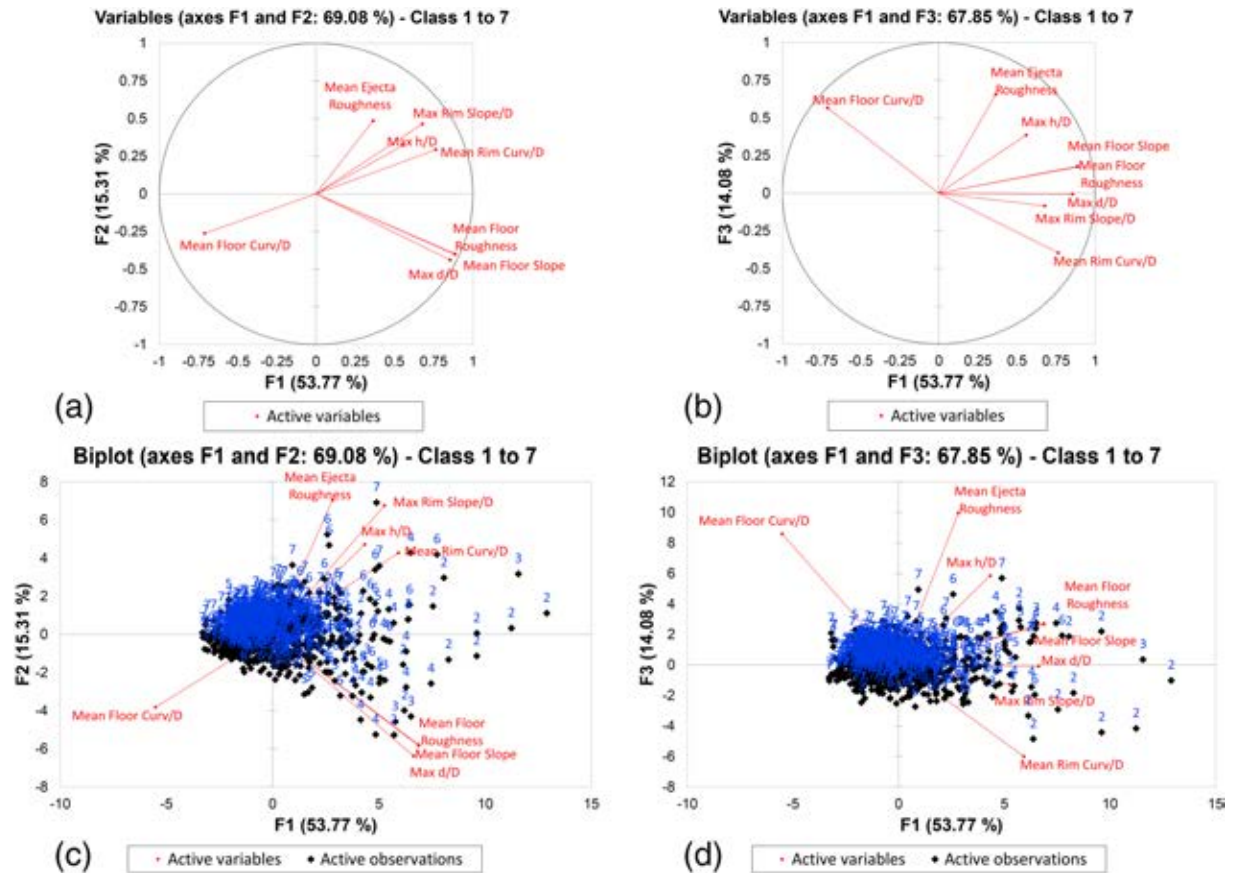


**Figure 18.** Results of the principal component analysis for all eight morphometric parameters for Classes 1 to 7 craters. (a) Correlation diagram showing components F1 and F2. The correlation circles provide vectors for the active variables (the morphometric parameters) in x,y principal component space and indicate which morphometric variables are most closely correlated. Low angles between the vectors indicate a significant positive correlation, orthogonal angles indicate no relationship, and obtuse angles suggest a negative correlation. A vector magnitude that is distal to the center of the circle indicates that the given principal components capture the bulk of the variability in the data. (b) Correlation diagram showing F1 and F3. Mean floor slope, mean floor roughness, and  $d/D$  are the most strongly correlated on both plots, similar to the Classes 1 to 8 analysis. (c, d) Biplots showing the distribution of the crater data plotted in principal component space. The freshest craters (Classes 2, 3, and 4) are clear end members, plotting along F1. The more degraded craters are clustered near the origin. The overall trend in the PCA analysis did not change with exclusion of the Class 8 hollows. Data points (black plus symbols) are labeled with the crater class (blue numbers).

that the older, Early Hesperian population of craters was resurfaced by ~200 m of basaltic lava (Golombek et al., 2018; Pan et al., 2019). Assuming a depth to diameter ratio of 0.2, ~200 m of lava would have completely resurfaced all craters on the landscape smaller than 1 km in diameter. The Early Amazonian age that is derived from the 100-m-scale population therefore reflects this resurfacing episode and is the most likely formation age of the Smooth Terrain that covers the InSight landing ellipse. The Early Amazonian age also represents the maximum possible age for the craters analyzed in the 21-km<sup>2</sup> study region surrounding InSight.

Crater degradation and erosion rates are provided for all diameter bins in Table 2. We focus primarily on Classes 5 to 8 craters because the statistics of fresher craters are poor and the time intervals between classes are not well constrained. Sweeney et al. (2018) report rates for Classes 1 to 5 craters at diameter ranges of 50, 100, 200, and 400 m. The time interval that separates a *Homestead hollow*-size, Class 5 crater from the Class 8 form is ~600 Myr (Table 1). The time interval to degrade a *Homestead hollow*-size crater to Class 5 is ~50 Myr. The timescales that separate each class are therefore not equal and imply a nonlinear decline in degradation rates through time. The average maximum depth of a Class 5 crater in the 25-m diameter bin is 1.2 m. Through Classes 6, 7, and 8, the average of the maximum crater depth changes from 0.79, to 0.59 m, and then to 0.45 m, respectively. Using the cumulative-derived time intervals between each class, this equates to degradation rates of  $4.6 \times 10^{-3} \text{ m Myr}^{-1}$  for Classes 5 to 6,  $1.2 \times 10^{-3} \text{ m Myr}^{-1}$  for Classes 6 to 7, and

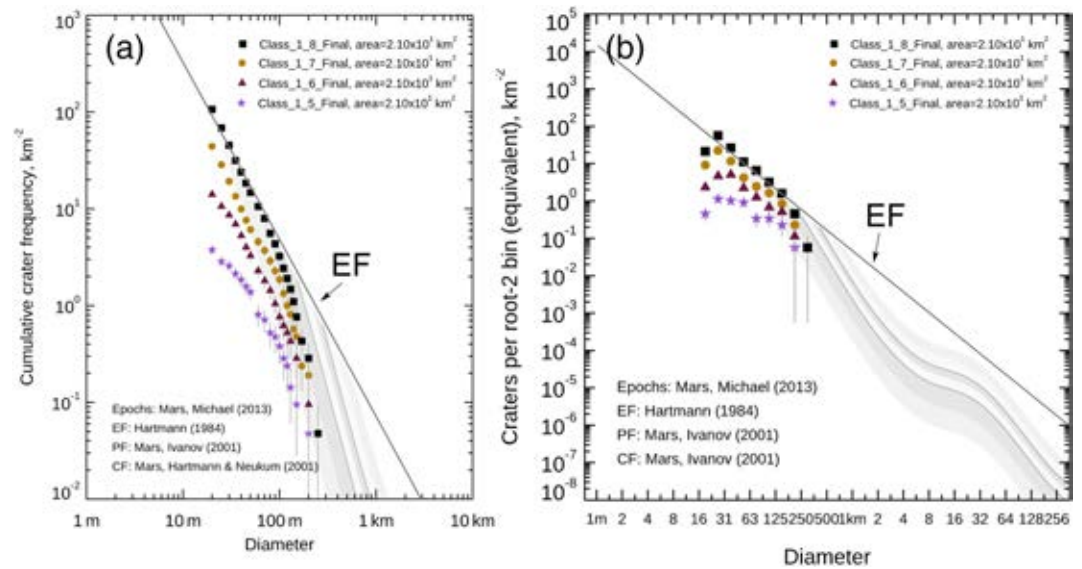


**Figure 19.** (a) Cumulative size-frequency histogram showing the distribution for Classes 1 to 5 (purple stars) craters, 1 to 6 (red triangles) craters, 1 to 7 (orange circles) craters, and 1 to 8 (black squares) craters/hollows. The chronology function of Hartmann and Neukum (2001), the production function (gray lines) of Ivanov (2001) and the equilibrium function (solid black line labeled equilibrium functions [EFs]) of Hartmann (1984) are plotted. The cumulative frequency at each bin (pseudo-log) was used to estimate a model age for different size craters in each class (see Table 1). (b) Incremental size-frequency distribution histogram for the same crater class groupings. The incremental plotting method is noncumulative and uses a square root of 2 bin. The same chronology, production, and EFs are shown.

$3.6 \times 10^{-4} \text{ m Myr}^{-1}$  for Classes 7 to 8. Similar order of magnitude rates are indicated for larger diameter bins. By comparison, Sweeney et al. (2018) estimated order of magnitude faster degradation rates ( $10^{-2} \text{ m Myr}^{-1}$ ) for Classes 1 to 5 craters that are  $\geq 50 \text{ m}$  in diameter. This indicates that craters degrade more quickly in the earlier stages of modification.

The average maximum rim height of Class 5, *Homestead hollow*-size craters, is 0.97 m. The rim heights change to 0.76 m for Class 6, 0.49 m for Class 7, and 0.34 m for Class 8. From the cumulative time intervals, the rim erosion rates are  $2.5 \times 10^{-3} \text{ m Myr}^{-1}$  for Classes 5 to 6,  $1.6 \times 10^{-3} \text{ m Myr}^{-1}$  for Classes 6 to 7, and  $4.1 \times 10^{-4} \text{ m Myr}^{-1}$  for Classes 7 to 8 (Table 2). The rim erosion rates are similar, if not identical within the error of the model ages ( $\pm 7$  to 90 Myr), to the crater degradation rates for craters older than Class 5. Alternatively, Sweeney et al. (2018) found consistently higher (by an order of magnitude) crater degradation rates ( $10^{-2} \text{ m Myr}^{-1}$ ) than rim erosion rates ( $10^{-3} \text{ m Myr}^{-1}$ ) for craters younger than Class 5. These, coupled with hillslope diffusion models, were used in that study to suggest that crater degradation within the InSight landing ellipse involved a significant component of sedimentary infill, in the form of windblown sand and externally derived ejecta. However, the data here indicate that the contribution of infill becomes relatively less important as a crater ages, likely due to the diminished capacity of the crater to trap saltating sand. Furthermore, rim erosion rates are comparable, if not slightly lower here than the Classes 1 to 5 examples. This suggests a comparatively lower and steadier decline in the rate of rim degradation through time.

## 5. Implications for Landing Site Observations and Near Surface Stratigraphy

### 5.1. The Smooth Surficial Unit

A smooth, sandy surface dominates the workspace and region immediately south and east of the lander (Figures 3 and 4; Golombek et al., 2020). The origin of this material is best explained in the context of the impact origin for *Homestead hollow* and the hollow's relative youth (Middle Amazonian retention age,  $\sim 400\text{--}700 \text{ Myr}$ ). Immediately outside of the hollow, pebble to cobble-size clasts of likely impact ejecta origin are more abundant, scattered on and within a sand-dominated regolith that was generated by  $\sim 2$  billion years of impact gardening and eolian modification (Golombek et al., 2018, 2020; Warner et al., 2017). The lack of large, 10-cm to 1-m-scale superposing ejecta blocks within the hollow indicates that it is a location

**Table 1**  
Data Derived From the Impact Crater Statistics (Figure 19), Including Number of Craters in Each Bin (Cumulative and Incremental), the Derived Model Ages, and the Errors for Those Model ages

Cumulative data																
Classes 1–5				Classes 1–6			Classes 1–7			Classes 1–8			Classes 5–8 interval	Classes 5–6 interval	Classes 6–7 interval	Class 7–8 Interval
Diameter bin (m)	Cum no./ bin	Age (Myr)	Error (±)	Cum no./ bin	Age (Myr)	Error (±)	Cum no./ bin	Age (Myr)	Error (±)	Cum no./ bin	Age (Myr)	Error (±)	Time (Myr)	Time (Myr)	Time (Myr)	Time (Myr)
20	79	40	5	296	110	6	929	240	8	2234	550	10	510	70	130	310
<b>25</b>	<b>60</b>	<b>53</b>	<b>7</b>	<b>223</b>	<b>140</b>	<b>10</b>	<b>599</b>	<b>300</b>	<b>10</b>	<b>1437</b>	<b>680</b>	<b>20</b>	<b>627</b>	<b>87</b>	<b>160</b>	<b>380</b>
30	54	67	9	181	180	10	404	360	20	952	790	30	723	113	180	430
35	45	80	10	146	210	20	283	410	20	662	900	30	820	130	200	490
40	39	94	10	111	240	20	209	480	30	502	1000	40	906	146	240	520
45	33	110	20	84	270	30	160	550	40	387	1100	60	990	160	280	550
50	29	130	20	69	310	40	128	640	60	309	1300	70	1170	180	330	660
60	17	150	40	48	360	50	96	750	80	222	1500	100	1350	210	390	750
70	15	170	40	38	410	70	77	860	100	167	1600	100	1430	240	450	740
80	11	190	60	30	450	80	61	930	100	117	1700	200	1510	260	480	770
90	10	210	70	22	470	100	48	990	100	91	1800	200	1590	260	520	810
100	8	220	80	16	500	100	39	1000	200	68	1800	200	1580	280	500	800
200	1	290	300	2	580	400	4	1200	600	6	1500	600	1210	290	620	300

Incremental data																
Classes 1–5				Classes 1–6			Classes 1–7			Classes 1–8			Classes 5–8 interval	Classes 5–6 interval	Classes 6–7 interval	Classes 7–8 interval
Diameter Bin	No./ Bin	Age (Myr)	Error (±)	No./ Bin	Age (Myr)	Error (±)	No./ Bin	Age (Myr)	Error (±)	No./ Bin	Age (Myr)	Error (±)	Time (Myr)	Time (Myr)	Time (Myr)	Time (Myr)
<b>22.1</b>	<b>20</b>	<b>15</b>	<b>2</b>	<b>82</b>	<b>55</b>	<b>3</b>	<b>396</b>	<b>170</b>	<b>6</b>	<b>992</b>	<b>400</b>	<b>9</b>	<b>385</b>	<b>40</b>	<b>115</b>	<b>230</b>
31.2	18	33	5	89	110	8	206	240	10	465	560	20	527	77	130	320
44.2	16	64	10	39	160	20	74	320	20	195	780	40	716	96	160	460
62.5	6	99	20	22	260	40	43	540	60	115	1200	80	1101	161	280	660
88.4	6	190	60	12	410	80	29	870	100	56	1600	200	1410	220	460	730
125	4	280	100	9	620	200	15	1100	200	28	2100	300	1820	340	480	1000
177	1	190	200	2	370	300	4	930	400	8	1700	600	1510	180	560	770

Note. Time intervals between each class are also shown. The time intervals were estimated by subtracting the calculated model ages between different classes. Model age errors similarly apply to the time intervals. The Hartmann and Neukum (2001) and Ivanov (2001) chronology and production functions were used to derive the model ages, respectively. The approximate *Homestead hollow*-size diameter bin is in bold. *Homestead hollow* bin in bold italics.

of preferential accumulation and/or preservation of fines and is entirely consistent with observations of sand accumulation inside of nearby fresher craters (Grant et al., 2020, this issue). The paucity of rocks is also consistent with the hollow's relatively young Middle Amazonian retention age. The crater retention and morphometry data indicate that the surface of *Homestead hollow* largely stabilized by Class 5 or 6, where the degradation and erosion rates converged at  $10^{-3}$  to  $10^{-4}$  m Myr<sup>-1</sup> (Table 2). This convergence indicates that almost all of the crater degradation at these stages occurred by very slow rates of rim erosion and that infilling had a near zero contribution to crater change. The time interval between degradation from Class 7 to the Class 8 morphology is the longest interval between sequential classes in the degradation series at ~200–400 Myr (incremental and cumulative intervals, respectively). The time interval between Classes 5 and 8 is ~400 to 600 Myr, respectively.

While the ejection of rocks into *Homestead hollow* likely began in the Middle Amazonian, there have been few impact events large enough or young enough that could have excavated and deposited large rocks onto the surface of the inner-hollow fill. *Rocky Field*, which drapes the western wall of the hollow (Golombek et al., 2020; Grant et al., 2020, this issue) may represent at least one, post-hollow rocky ejecta event. *Rocky Field* appears to fully superpose the fill of the hollow (Grant et al., 2020, this issue) indicating that the

**Table 2**  
Crater Degradation and Crater Erosion Rate Data for Various Class Intervals

Crater degradation rates								
Diameter bin (m)	Classes 5–8		Classes 5–6		Classes 6–7		Classes 7–8	
	Deg. rate (m/Myr)	Error (±)	Deg. rate (m/Myr)	Error (±)	Deg. rate (m/Myr)	Error (±)	Deg. rate (m/Myr)	Error (±)
20	3.7E-04	1.1E-05	NA	NA	1.3E-03	1.5E-04	1.2E-04	7.2E-06
<b>25</b>	<b>1.2E-03</b>	<b>5.2E-05</b>	<b>4.6E-03</b>	<b>1.1E-03</b>	<b>1.2E-03</b>	<b>1.7E-04</b>	<b>3.6E-04</b>	<b>3.0E-05</b>
30	9.0E-04	5.2E-05	2.7E-03	5.4E-04	1.3E-03	2.5E-04	2.9E-04	3.8E-05
35	1.6E-03	8.3E-05	4.6E-03	1.4E-03	2.4E-03	6.0E-04	5.2E-04	5.9E-05
40	1.4E-03	7.9E-05	2.6E-03	6.6E-04	2.5E-03	6.5E-04	4.9E-04	7.7E-05
45	1.4E-03	1.2E-04	2.5E-03	1.1E-03	2.0E-03	6.7E-04	7.4E-04	1.6E-04
50	1.9E-03	1.6E-04	5.9E-03	2.9E-03	1.7E-03	7.3E-04	8.7E-04	2.1E-04
60	2.1E-03	2.4E-04	8.4E-03	6.3E-03	1.4E-03	6.8E-04	6.9E-04	2.2E-04
70	2.2E-03	2.4E-04	6.7E-03	5.7E-03	2.3E-03	1.4E-03	7.0E-04	2.6E-04
80	NA	NA	NA	NA	1.0E-03	6.1E-04	1.2E-03	7.8E-04
90	2.1E-03	4.3E-04	9.6E-03	1.8E-02	3.6E-04	2.3E-04	8.0E-04	4.7E-04
100	2.5E-03	5.5E-04	6.1E-03	1.1E-02	3.6E-03	5.4E-03	6.6E-04	6.6E-04
200	NA	NA	NA	NA	1.3E-03	3.4E-03	1.0E-02	1.4E-02

Crater erosion rates								
Diameter bin (m)	Classes 5–8		Classes 5–6		Classes 6–7		Classes 7–8	
	Erosion rate (m/Myr)	Error (±)	Erosion rate (m/Myr)	Error (±)	Erosion rate (m/Myr)	Error (±)	Erosion rate (m/Myr)	Error (±)
20	6.6E-04	2.0E-05	NA	NA	1.8E-03	2.2E-04	4.3E-04	2.7E-05
<b>25</b>	<b>1.0E-03</b>	<b>4.5E-05</b>	<b>2.5E-03</b>	<b>6.0E-04</b>	<b>1.6E-03</b>	<b>2.3E-04</b>	<b>4.2E-04</b>	<b>3.6E-05</b>
30	1.3E-03	7.4E-05	4.3E-03	8.7E-04	1.1E-03	2.2E-04	5.8E-04	7.6E-05
35	1.2E-03	5.9E-05	2.9E-03	8.6E-04	1.8E-03	4.5E-04	4.4E-04	5.0E-05
40	7.9E-04	4.6E-05	2.1E-03	5.5E-04	8.6E-04	2.3E-04	3.8E-04	5.9E-05
45	9.4E-04	8.3E-05	2.9E-03	1.3E-03	2.6E-04	8.7E-05	7.3E-04	1.6E-04
50	8.2E-04	6.8E-05	1.8E-03	8.9E-04	1.6E-04	6.9E-05	8.9E-04	2.2E-04
60	9.7E-04	1.1E-04	3.9E-03	2.9E-03	3.0E-05	1.5E-05	6.4E-04	2.0E-04
70	1.4E-03	1.5E-04	5.6E-03	4.8E-03	NA	0.0E+00	8.2E-04	3.0E-04
80	NA	NA	NA	NA	NA	0.0E+00	NA	0.0E+00
90	3.2E-06	6.6E-07	7.9E-05	1.5E-04	NA	0.0E+00	1.2E-03	7.0E-04
100	1.9E-03	4.2E-04	7.1E-03	1.3E-02	1.3E-03	1.9E-03	5.2E-04	5.2E-04
200	NA	NA	NA	NA	NA	0.0E+00	7.4E-03	9.8E-03

Note. The data were derived using the model ages and time intervals from the cumulative fits for consistency with Sweeney et al. (2018). Errors account for model age uncertainties. The approximate *Homestead hollow*-size diameter bin is in bold. Rate data assumes the cumulative-derived model ages.

rocks were emplaced after the fill materials stabilized (Figures 3 and 4). The continuous ejecta blankets of nearby craters are shown in Figure 16, superposed on a rock map generated by manual counts using the HiRISE image. Rocks of the size observed in *Rocky Field* (order of 10 cm) are not visible at HiRISE resolution. The ejecta and rock map indicate that *Homestead hollow* is not within range of the continuous ejecta of any fresh, RECs. Grant et al. (2020, this issue) identifies a degraded, 155-m-diameter crater that is 200 m northwest of *Homestead hollow* as a possible source for *Rocky Field*. From our analysis, this crater is a Class 6 crater with a maximum landscape retention age of ~400 to 600 Myr. This impact could feasibly postdate *Homestead hollow* and its infill. At 155 m, the Class 6 crater is also large enough to have excavated through the regolith (Warner et al., 2017; Golombek et al., 2020), reaching the rock at depth. Ejecta from far field impact events also cannot be ruled out as the source for the rocks in *Rocky Field*.

### 5.2. Origin of the Duricrust

Pits excavated by InSight's retro-rockets (Figure 4), as well as the apparent slope stability of the HP<sup>3</sup> mole hole (Figure 20), indicate mild cohesion of the upper ~5 to 10 cm of the sandy soil inside *Homestead hollow* (Golombek et al., 2020; Ansan et al., 2019). This soil horizon is interpreted to be a duricrust, produced by the long-term and relatively slow exchange of atmospheric water vapor with soil. Salts (e.g., sulfates), deposited as a result of this exchange, are the most likely cohesive agent (Vaniman et al., 2004; Yen et al., 2005;

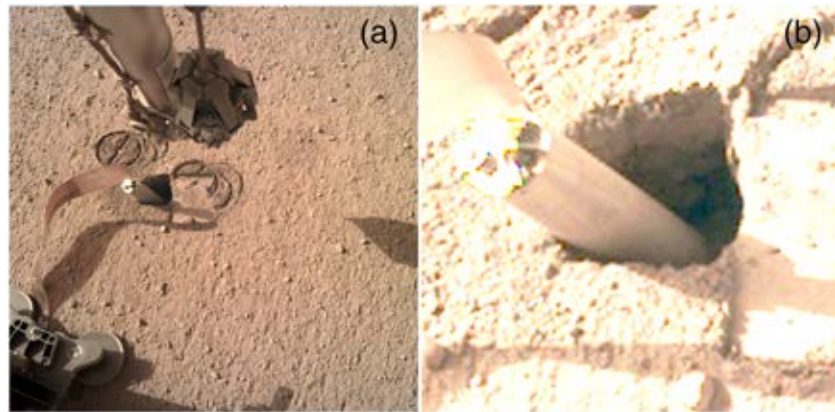


**Figure 20.** (a) Instrument Deployment Camera (IDC) image D000M0243\_618084024EDR\_F0000\_0800M taken on Sol 243 of the HP<sup>3</sup> mole hole following mole penetration. The mole is 2.7 cm in diameter (Spohn et al., 2018). (b) Contrast-stretched IDC image showing a zoomed in view of the mole hole. The walls of the hole are relatively steep, above the angle of repose for fine sand ( $\sim 30^\circ$ ). This, combined with the lack of observed hole collapse during penetration, suggests cohesion in the upper few centimeters of the fill inside of *Homestead hollow*. This cohesive material is interpreted to be a duricrust (Golombek et al., 2020).

Martín-Torres et al., 2015). Duricrust, or weakly cohesive soils, are not unique to the InSight landing site. Duricrust has been described from orbital thermal data (e.g., Christensen et al., 2001; Jakosky & Christensen, 1986) and from the ground by the Viking landers (Binder et al., 1977; Mutch et al., 1977; Jones et al., 1979; Arvidson et al., 1989), Mars Pathfinder (Moore et al., 1999), the Mars Exploration Rovers (Arvidson et al., 2010; Cabrol et al., 2006; Fergason et al., 2006; Golombek, Crumpler, et al., 2006), and the Mars Science Laboratory (Arvidson et al., 2014). Here we argue that the formation and thickness of the duricrust is directly attributable to sediment trapping and the establishment of a relatively old and stable soil within *Homestead hollow*.

The morphometry and crater data indicate a near zero crater fill rate as craters degrade from Classes 5 to 8, a time interval of approximately  $\sim 400$  to 600 Myr (Table 1). A comparison of the depths of *Homestead-hollow-size* Classes 5 and 8 craters confirms minimal change over this period. Approximately 0.7 cm of depth-related change occurs within a 25-m diameter crater between the Classes 5 and 8 states. However,  $\sim 0.6$  cm of that depth change is accommodated by rim erosion. Soil stability for (order of) 100 Myr could facilitate relatively thick duricrust formation through pervasive, yet likely episodic, diffusion of water vapor into the soils. Furthermore, multiple high obliquity cycles likely occurred over this time (Forget et al., 2006; Head et al., 2003; Jakosky & Carr, 1985; Madeleine et al., 2014; Mischna & Richardson, 2005) and may be responsible for enhanced vapor deposition at equatorial latitudes. The interiors of Classes 5 to 8 craters all exhibit similar smooth infilling materials that might contain a surficial duricrust. HiRISE images reveal that the infill may be somewhat indurated by the Classes 4 and 5 morphologic stage (Figure 21). Escarpments are present in the smooth infill at locations where the material has either been partially degraded or has incompletely stabilized. In addition, the infill retains small craters that exhibit well-defined rims, bowl-shaped morphology, and in some cases, ejecta (Figures 8 and 21). The classification from Classes 5 to 8 is noted for the ever increasing abundance of superposing 1- to 10-m-size craters on the infill, confirming long retention timescales and soil stability.

The question remains as to whether multiple duricrust horizons exist at depth in the hollow, representing hiatuses during the younger stages of crater degradation. The presence of eolian bedforms at multiple scales of evolution would suggest that the morphology/deposition of crater fill materials is transient from Classes 1 to 3, precluding the establishment of thick duricrust horizons. The thickest package of duricrust therefore should be present within only the uppermost horizon(s) of the fill, formed after the fill stabilized. The presence of dust-mantled bedforms within and surrounding fresh Classes 2, 3, and 4 craters in the study region however suggests that the modern wind regime is below the critical threshold for sand transport and that the fill, even in fresh craters, is currently stable. This is supported by a year of surface observations at the landing site that have shown extremely limited surface changes or movement of clasts in the workspace or on lander

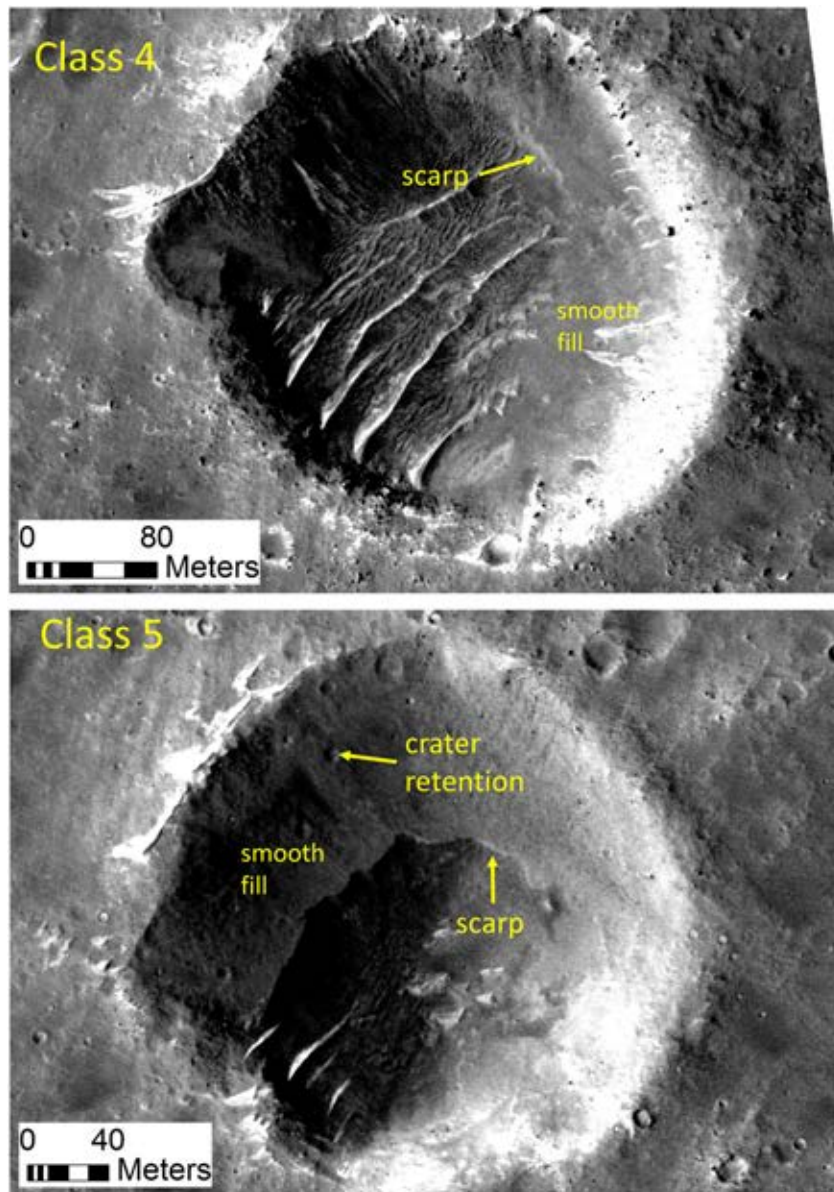


**Figure 21.** HiRISE image ESP\_042405\_1845 from within the InSight landing ellipse showing examples of the smooth fill in a Class 4 (a) and Class 5 (b) crater. In these craters, the smooth fill has either been partially degraded or is in a transient state of formation. The smooth interior materials form a scalloped, elevated escarpment that might indicate induration. Well-preserved impact craters are also evident. North is up on both images and illumination is from the left.

hardware, although some traction transport of  $\sim 3$ -mm-size grains has been observed (Baker et al., 2019). In order for the degradational sequence to continue for the nearby fresh craters, transport thresholds must be exceeded. This may require exposure of additional fines via impact events or a different climate regime than today. High obliquity cycles, which occur over time intervals of  $\sim 10^5$  years, have the potential to increase the atmospheric pressure on Mars by one to two orders of magnitude by sublimating the perennial north and south polar ice caps (Forget et al., 2006; Head et al., 2003; Jakosky & Carr, 1985; Madeleine et al., 2014; Mischna & Richardson, 2005). It is possible that such cycles trigger episodic motion of available sand (e.g., sand not trapped within hollows or between rocks on surrounding rims), which when integrated over 10 to 100 Myr, results in steady, long-term filling. A similar mechanism was attributed to the apparent ancient ( $\sim 50$ –200 Ka) migration of plains ripples at Meridiani Planum (Fenton et al., 2018; Golombek et al., 2010).

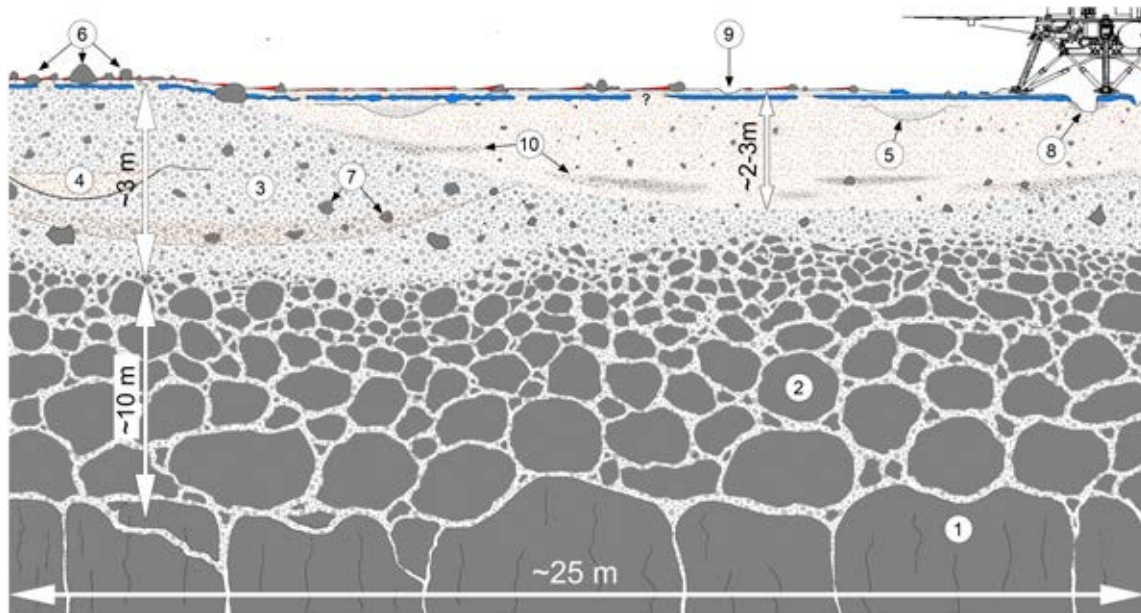


**Figure 22.** Schematic of the inferred regolith stratigraphy beneath the InSight lander, revised from Golombek et al. (2020). (1) fractured basaltic bedrock at a depth of ~10 to 20 m. Depth inferred using the onset diameter of 100-m-scale rocky ejecta craters in the landing site (Golombek et al., 2018; Warner et al., 2017). (2) fractured, coarse regolith at a depth of ~3 to 10 m. Smaller, 60 to 100 m size craters in the landing site exhibit evidence in HiRISE images for discontinuous rocky ejecta, indicating excavation of meter-size rocks from depths of <10 m (Warner et al., 2017). (3) Granular regolith unit dominated by pebble, sand, and cobble-size clasts with occasional boulders at depths of <3 m. An upper, finer horizon of regolith is likely present across the landing site based on observations of concentric craters and the identification of small ( $D < 60$  m), pristine, nonrocky ejecta craters (Warner et al., 2017). Lander-based observations confirm the presence of a relatively boulder-free, sand, pebble, and cobble-dominated surficial regolith on the intercrater plains (Golombek et al., 2020; Grant et al., 2020, this issue). (4) Buried impact crater with sandy fill. Eolian filling occurs immediately after formation of impact craters. A similar sand-dominated fill occurs inside of *Homestead hollow*. (5) Impact craters superposed on and within the fill of *Homestead hollow*. At *Homestead hollow*, the majority of these craters superpose the margins of the impact structure. Few buried craters likely exist at depth within the fill of the hollow due to early stage, rapid infilling. (6) Superposed cobble and boulder-size rocks. These float rocks were either derived from impact events (e.g., *Rocky Field*) and/or represent rocks that were ejected during the formation of the hollow. (7) Cobble to boulder-size rocks buried within the upper regolith column. Few rocks of this size are present within the hollow owing to its relatively young age in comparison to nearby large, rock-producing impacts. (8) Pits excavated by the lander's retro-rockets (see Golombek et al., 2020; Grant et al., 2020, this issue; Ansan et al., 2019). These 10-cm-deep pits expose a mildly cohesive, centimeters-thick duricrust horizon. (9) Shallow, 10-mm to 1-cm-deep divot produced by the *Rolling Stones* rock (Golombek et al., 2020). This rock was transported by rocket energy during decent, impacted the regolith, and exposed a fine-grained, non-cohesive, sand-dominated upper horizon. Microns of dust superpose this horizon—although much of the dust was removed during landing (Williams et al., 2019). (10) Coarser lenses of slope debris. This debris is derived from mass wasting along the interior margin of *Homestead hollow*.

### 5.3. Thickness and Stratigraphy of the Fill

The impact origin for *Homestead hollow* and the observed local degradational sequence provides morphometric constraints on the depth of fill and therefore the minimum thickness of the surficial granular regolith at this location (Figure 22). *Homestead hollow* is ~27 m in diameter. However, slope backwasting occurred during degradation, a result of hillslope modification. Hillslope diffusion models for this location (Sweeney et al., 2018) suggest up to ~20% widening during degradation to Class 5. Assuming 20% widening and a pristine depth to diameter ratio of  $d = 0.15D$  (Sweeney et al., 2018), *Homestead hollow* originated as a ~22-m diameter impact crater with a pristine depth of ~3.3 m. The current maximum depth of *Homestead hollow* is ~0.3 m. This suggests ~3 m of total degradation since formation. The maximum rim height of *Homestead hollow* in its pristine state, using the  $h = 0.03D$  relationship from Sweeney et al. (2018), is ~0.7 m, although the maximum average rim height in this analysis is ~1.0 m for craters in the 25-m-diameter bin. The current rim height of *Homestead hollow* is variable, ranging from zero on the northwest rim to ~0.2 m on the southeast rim. Regardless, the total amount of observed degradation cannot be accounted for solely by rim erosion. We therefore estimate ~2 to 3 m of sedimentary fill inside of the hollow. This is consistent with the overall regolith thickness of ~3 m at this location in Elysium Planitia (Warner et al., 2017; Golombek et al., 2018, 2020). The consistency between these two depths speaks to the potential importance of not only impact gardening by  $\geq 10$ -m-scale craters, but crater filling in the production of a meters-thick granular regolith.

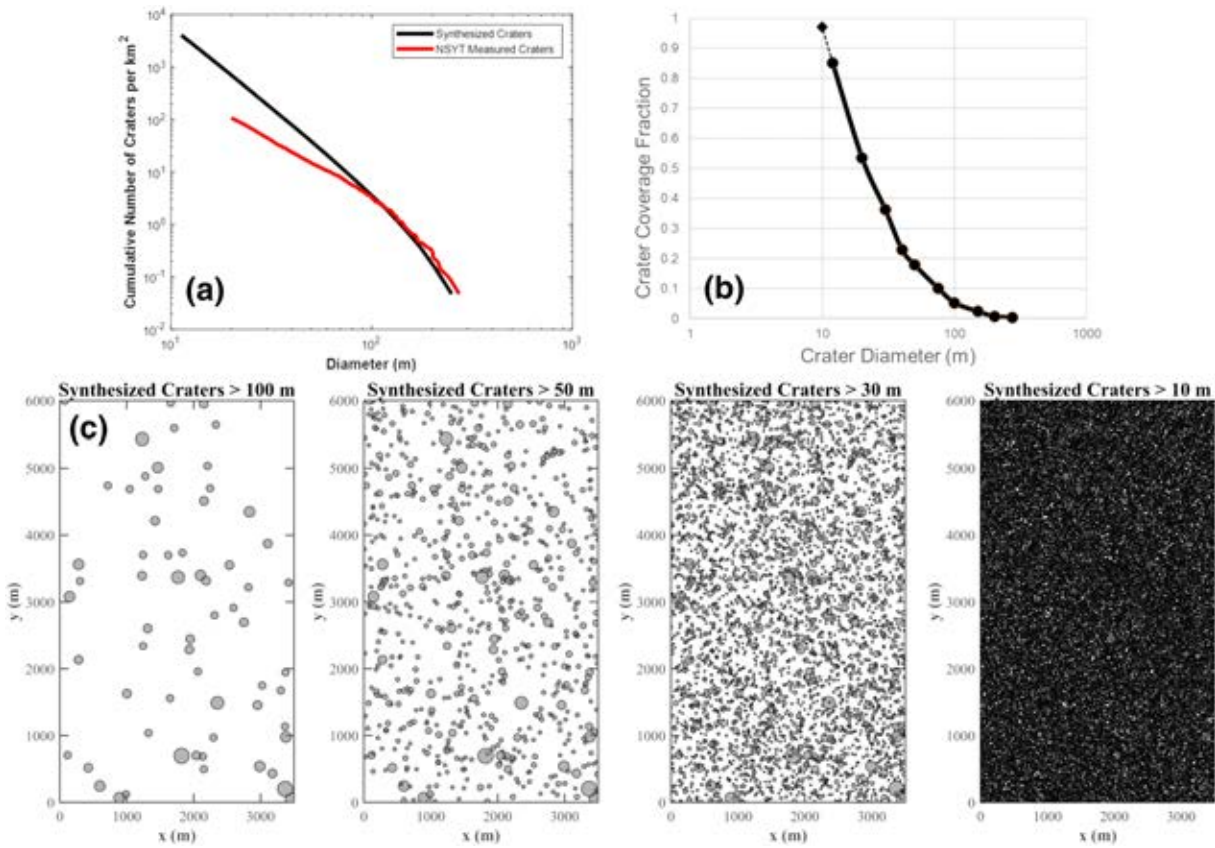


**Figure 23.** (a) Cumulative size-frequency distribution of the measured population of craters at InSight (NSYT measured) compared against a synthesized production population produced by extrapolating the  $-3.2$  (near) power law production slope for craters with  $D \geq 100$  m down to 10-m-size impacts. In reality, the measured population at  $D \leq 100$  m follows a near  $-2$  slope that approaches the crater equilibrium function (Hartmann, 1984). (b) Percent area coverage graph for each diameter bin derived from the synthesized crater population. The simulated  $21 \text{ km}^2$  area is nearly 100% saturated by impactors with  $D \geq 10$  m. (c) The synthesized crater distributions for different diameter bins visualizing the area covered by impact craters.

The stratigraphic architecture of the regolith beneath the lander can also be constrained through a combination of regional geologic analyses and by inferring the most likely processes for crater filling. The crater itself likely impacted into a preexisting, sand-dominated granular regolith that had developed at this location via impact fragmentation over a timespan of  $\sim 1.0$  to  $1.3$  billion years, assuming a  $\sim 400$  to  $700$  Myr retention age for *Homestead hollow* and a  $\sim 1.7$  Gyr maximum age for the Smooth Terrain (Warner et al., 2017). Figure 16 illustrates the overlap of observed,  $\geq 20$  m in diameter craters. Craters in this size range occupy  $\sim 16\%$  of the total area in the study region, including spatial overlap. The ejecta, with overlap, occupies  $\sim 78\%$  of the area. However, the observed distribution of 10-m-scale craters is not representative of a production population, rather a population in equilibrium with destructive surface processes. Figure 23a compares the equilibrium slope for Classes 1 to 8 craters against a simulated production population, assuming no degradation and no secondary clusters (i.e., Corinto secondaries—see Golombek et al., 2017), for a surface of similar age to the Smooth Terrain (1.7 Gyr). A (near) production power law slope of  $-3.2$  was extrapolated for the  $D \leq 100$  m population, derived from the measured slope of the  $D \geq 100$  m population. This slope is similar to the  $-3.5$  to  $-3.0$  cumulative production slopes of Ivanov (2001) and Hartmann and Daubar (2016) for craters with diameters between 10 and 500 m. While such a surface is unlikely on Mars (Hartmann, 1984), the simulation serves to better understand the total number of possible impact events that may have shaped the landscape at the landing site and thus helps infer near surface stratigraphic characteristics. Figure 23b highlights the percent area covered by the production population over a simulated  $\sim 21\text{-km}^2$  surface. The simulated craters are also shown graphically (Figure 23c). The data demonstrates that a surface with a maximum exposure age of  $\sim 1.7$  Gyr approaches true saturation at  $D \geq 10$  m, assuming random



overlap. Using a pristine  $d/D$  of 0.15 (Sweeney et al., 2018), the saturation diameter threshold indicates that the lava plains here have been completely reworked by impact events to a depth of at least  $\sim 1.5$  m. The ejecta from these impacts also oversaturated the surface, replacing the preexisting bedrock with centimeters to meters of loose, fragmented materials. The upper few meters of the target material for the *Homestead hollow* impact, with an exposure age of  $\sim 1.0$  to 1.3 Gyr, were more than likely composed of a loose regolith; a combination of preexisting ejecta and filled crater cavities. Thicker regolith likely exists proximal to and within 100-m-scale craters that have been filled by tens of meters of loose material. Locally, thin regolith must be present at locations that by random probability, did not experience impacts or fill. Analysis of the size, age, and ejecta extent of craters that pre-date *Homestead hollow* indicate that the impactor struck the continuous ejecta of a larger and older 102-m-size Class 7 crater that is located just northeast of the landing site (Figure 16). The estimated retention age of a 100-m-sized Class 7 crater is  $\sim 0.9$ –1.0 Gyr. The crater is large enough to have fully excavated through the granular regolith and into the rockier materials at depth (Warner et al., 2017). It is therefore possible that *Homestead hollow* rests on top of remnants of the rocky ejecta of this impact structure.

Given the size, depth, and target property constraints of *Homestead hollow*, the ejecta and crater rim walls were (and still are) likely composed of loose, granular materials. The crater rim and walls therefore would have been subject to relatively rapid rim degradation by hillslope creep, granular flow-style mass wasting, eolian transport, and degradation by subsequent impacts. Slope transport of the rim material likely created small, meter-scale debris aprons of loose sand, granules, pebbles, and isolated cobbles. This material should be thickest at the basal contact of the hollow (Figure 22). Following formation of the crater, the ejecta of *Homestead hollow* formed a slightly elevated surface of loose debris, which would have been immediately in disequilibrium with the local wind regime. Sand-size materials would have been mobilized soon after impact as a result and filling by windblown sand would have occurred during the same time that slope modification was generating interior debris aprons. Coarser materials, derived from mass wasting, should therefore interfinger cross-laminated, cross-bedded, and horizontally stratified eolian sands in the stratigraphic section of the interior hollow (Figure 22). Sand-size materials derived from other impacts would have been ejected into the crater at all phases. By Class 5, the morphologic observations indicate that bedforms should no longer be present on the floor of the crater. This is likely due to a reduced capacity for sediment trapping as the crater becomes more subdued and the degradation of the bedforms (Figure 6). The processes that caused smoothing of the infill by Class 5 are unknown. Once stable, bedforms could plane off by slow granular creep along all of their sloping margins and/or more punctuated mass wasting along their steeper slip faces. In addition or alternatively, ongoing dust airfall and impact ejecta could bury stabilized bedforms, filling the troughs between the crests. It is unclear whether dust was a significant contributor to crater filling here. Orbital and ground-based thermal inertia from the Radiometer instrument is only sensitive to the upper few centimeters of regolith (Mueller et al., 2019). At these depths, the overall region and the landing site itself exhibit only a microns-thick dust horizon (Golombek et al., 2020). The TWINS atmospheric experiment has detected multiple, low pressure vortices at the landing site that could be responsible for dust mobilization, lifting, and dust devil formation (Banfield et al., 2020). HiRISE images reveal a landscape that is riddled with dust devil tracks (Reiss & Lorenz, 2016). However, no dust devils have been observed through the first Earth year of InSight observations (Banfield et al., 2020), despite detections of strong low-pressure vortices. This indicates that if dust is present here, it may either be in low abundance at the surface or is intermixed with coarser materials and possibly protected from lifting by vortices.

Following infill stabilization through Classes 5 and 8, the thick duricrust horizon was likely generated and superposing impact craters were retained in increasing density on the fill. The described stratigraphy (Figure 22) is generally consistent with the results of the HP<sup>3</sup>-SEIS hammering experiment that detected a low velocity zone in at least the upper 1 m of the surface beneath the lander (Kedar et al., 2017; Lognonné et al., 2020). This zone most likely corresponds with the loose, granular, and likely porous hollow fill materials. InSight rests on the northwest margin of the hollow where the fill is likely shallower than the estimated maximum thickness of  $\sim 3$  m. A higher seismic wave velocity zone is indicated below these depths. The velocity values are however inconsistent with solid bedrock, and are likely the result of a transition from hollow fill to underlying rockier materials, possibly representing ejecta from the preexisting impact of the nearby Class 7 crater (Figure 16).

## 6. Conclusions

Crater morphometric data and the SFD of all Classes 1 to 8 craterforms strongly support the hypothesis that *Homestead hollow*, a ~27-m-diameter, quasi-circular depression and the landing location of the InSight lander, is a degraded impact crater. The hollow is representative of the most degraded crater in a degradation continuum established by Sweeney et al. (2018) for Classes 1 to 5 RECs and expanded here to include smaller and more degraded Classes 6 to 8 craters. Crater statistics indicate that the maximum age of *Homestead hollow* is ~400 to 700 Myr. The morphometric data confirms that *Homestead hollow* crater degraded by a combination of rim destruction and infill. Rim destruction can be entirely explained by gravity-driven mass wasting (Sweeney et al., 2018), which reduced the rim height, the rim slope, and maintained rim convexity through time. Post-hollow impact events and eolian abrasion are also likely contributors to degradation. Crater fill can be explained by a combination of eolian transport of sand, accumulation of slope debris, and delivery of externally derived ejecta. Eolian processes had an apparently larger influence on crater filling at the earliest stages of crater formation where the crater served as a sediment trap for migrating sand. The total estimated fill for the hollow, assuming a pristine depth of ~3 m and rim height of ~1 m, is ~2 to 3 m. The time dependence of these processes is reflected in the derived degradation rates, which decrease by two orders of magnitude for 10-m-scale craters through their lifetime from  $10^{-2}$  to  $10^{-4}$  m Myr<sup>-1</sup>. Rim erosion rates decreased over their lifetime by one order of magnitude from  $10^{-3}$  to  $10^{-4}$  m Myr<sup>-1</sup>. These rates are consistent with Hesperian to Amazonian-age erosion rates calculated elsewhere on Mars (Golombek, Grant, et al., 2006; Golombek et al., 2014), and across the broader landscape of the ellipse (Sweeney et al., 2018). A convergence of the degradation rates and rim erosion rates occurs once the Class 5 morphologic state is reached and implies that the bulk of the material filled the crater of *Homestead hollow* by Class 5, within the first ~50 Myr after crater formation. This early filling not only limits the number of rock-producing impacts that could have deposited large blocks into the hollow while it was filling but facilitates the presumably slow formation of a duricrust within stable, surficial soils that were exposed to the atmosphere over the remaining ~600 Myr of the crater's history. These observations collectively provide constraints for ongoing geophysical investigations at the landing site.

### Acknowledgments

Warner's contribution was supported through the NASA Participating Scientist program under Grant 80NSSC18K1624. Grant, Wilson, and Weitz's contributions were supported through the NASA Participating Scientist program under Grant 80NSSC18K1625. A portion of the work was also supported by the InSight Project at the Jet Propulsion Laboratory, California Institute of Technology, under a contract with the National Aeronautics and Space Administration. We are especially grateful to the Mars Reconnaissance Orbiter HiRISE (University of Arizona) and CTX (Malin Space Science Systems) imaging teams for their high quality data and hard work in acquiring InSight imagery. HiRISE, CTX, THEMIS, and InSight lander-based imagery are available through the NASA Planetary Data System (<https://pds.nasa.gov/>). HiRISE data can be accessed through the University of Arizona at <https://hirise.lpl.arizona.edu/>. All crater morphometry data relevant to the morphometric and crater counting results of this study are available in supporting information Data Set 1 hosted at <https://doi.org/10.6084/m9.figshare.11916486.v1>. All regression statistics are available in supporting information Data Set 2 hosted at <https://doi.org/10.6084/m9.figshare.11916489.v1>. This paper is InSight Contribution Number 145. We would like to thank Jay Dickson and an anonymous reviewer for their thorough and helpful reviews.

## References

- Ansan, V., Hauber, E., Golombek, M., Warner, N., Grant, J., Maki, J., et al. (2019). InSight landing site: Stratigraphy of the regolith beneath the lander and in its surroundings, and implications for formation processes, 50th Lunar and Planetary Science, Abstract #1310.
- Armitage, J. J., Warner, N. H., Goddard, K., & Gupta, S. (2011). Timescales of alluvial fan development by precipitation on Mars. *Geophysical Research Letters*, 38, L17203. <https://doi.org/10.1029/2011GL048907>
- Arvidson, R., Boyce, J., Chapman, C., Cintala, M., Fulchignoni, M., Moore, H., et al. (1979). Standard techniques for presentation and analysis of crater size-frequency data. *Icarus*, 37, 467–474.
- Arvidson, R. E., Bell, J. F. III, Bellutta, P., Cabrol, N. A., Catalano, J. G., Cohen, J., et al. (2010). Spirit Mars rover mission: Overview and selected results from the northern Home Plate Winter Haven to the side of Scamander crater. *Journal of Geophysical Research*, 115, E00F03. <https://doi.org/10.1029/2010JE003633>
- Arvidson, R. E., Bellutta, P., Calef, F., Fraeman, A. A., Garvin, J. B., Gasnault, O., et al. (2014). Terrain physical properties derived from orbital data and the first 360 sols of the Mars science laboratory curiosity rover observations in Gale crater. *Journal of Geophysical Research: Planets*, 119, 1322–1344. <https://doi.org/10.1002/2013JE004605>
- Arvidson, R. E., Gooding, J. L., & Moore, H. J. (1989). The Martian surface as imaged, sampled, and analyzed by the Viking landers. *Reviews of Geophysics*, 27(1), 39–60. <https://doi.org/10.1029/RG027i001p00039>
- Baker, M. M., Newman, C. E., Charalambous, C., Banfield, D., Golombek, M. P., Garvin, J., et al. (2019). Aeolian change detection from the InSight lander. *GSA Abstracts with Programs*, 51, No. 5. <https://doi.org/10.1130/abs/2019AM-341098>
- Banerdt, W. B., Smrekar, S. E., Banfield, D., Giardini, D., Golombek, M., Johnson, C. L., et al. (2020). Early results from the InSight mission on Mars. *Nature Geoscience*, 13(3), 183–189. <https://doi.org/10.1038/s41561-020-0544-y>
- Banfield, D., Spiga, A., Newman, C., Forget, F., Lemmon, M., Lorenz, R., et al. (2020). The atmosphere of Mars as observed by InSight. *Nature Geoscience*, accepted, 13(3), 190–198. <https://doi.org/10.1038/s41561-020-0534-0>
- Binder, A. B., Arvidson, R. E., Guinness, E. A., Jones, K. L., Morris, E. C., Mutch, T. A., et al. (1977). The geology of the Viking Lander 1 site. *Journal of Geophysical Research*, 82(28), 4439–4451. <https://doi.org/10.1029/JS082i028p04439>
- Bloom, C., Golombek, M., Warner, N., & Wigton, N. (2014). Size frequency distribution and ejection velocity of Corinto crater secondaries in Elysium Planitia, in Eighth International Conference on Mars, Pasadena, CA, July 14–18, Lunar and Planetary Institute, Houston, Abstract #1289.
- Cabrol, N. A., Farmer, J. D., Grin, E. A., Richter, L., Soderblom, L., Li, R., et al. (2006). Aqueous processes at Gusev crater inferred from physical properties of rocks and soils along the Spirit traverse. *Journal of Geophysical Research*, 111, EOZS20. <https://doi.org/10.1029/2005JE002490>
- Charalambous, C., Golombek, M., Pike, T., Warner, N. H., Weitz, C., Ansan, V., et al. (2019). Rock distributions at the InSight landing site and implications based on fragmentation theory, 50th Lunar and Planetary Science, Abstract #2812.
- Christensen, P. R., Bandfield, J. L., Hamilton, V. E., Ruff, S. W., Kieffer, H. H., Titus, T. N., et al. (2001). Mars global surveyor thermal emission spectrometer experiment: Investigation description and surface science results. *Journal of Geophysical Research*, 106(E10), 23,823–23,871. <https://doi.org/10.1029/2000JE001370>

- Craddock, R. A., & Howard, A. D. (2000). Degraded Noachian craters: Fluvial versus lava infilling, 31st Lunar Planet. Sci. Conf., Abstract 1542.
- Craddock, R. A., Maxwell, T. A., & Howard, A. D. (1997). Crater morphology and modification in the Sinus Sabaeus and Margaritifer Sinus regions of Mars. *Journal of Geophysical Research*, *102*(E6), 13,321–13,340. <https://doi.org/10.1029/97JE01084>
- Daubar, I. J., Atwood-Stone, C., Byrne, S., McEwen, A. S., & Russell, P. S. (2014). The morphology of small fresh craters on Mars and the Moon. *Journal of Geophysical Research: Planets*, *119*, 2620–2639. <https://doi.org/10.1002/2014JE004671>
- Fassett, C. I., & Thomson, B. J. (2014). Crater degradation on the lunar maria: Topographic diffusion and the rate of erosion on the Moon. *Journal of Geophysical Research: Planets*, *119*, 2255–2271. <https://doi.org/10.1002/2014JE004698>
- Fenton, L. K., Carson, H. C., & Michaels, T. I. (2018). Climate forcing of ripple migration and crest alignment in the last 400 kyr in Meridiani Planum, Mars. *Journal of Geophysical Research: Planets*, *123*, 849–863. <https://doi.org/10.1002/2017JE005503>
- Ferguson, R. L., Christensen, P. R., Bell, J. G. III, Golombek, M. P., Herkenhoff, K. E., & Kieffer, H. H. (2006). Physical properties of the Mars exploration rover landing sites as inferred from mini-TES-derived thermal inertia. *Journal of Geophysical Research*, *111*, E02S21. <https://doi.org/10.1029/2005JE002583>
- Ferguson, R. L., Kirk, R. L., Cushing, G., Galuzska, D. M., Golombek, M. P., Hare, T. M., et al. (2017). Analysis of local slopes at the InSight landing site on Mars. *Space Science Reviews*, *211*(1–4), 109–133. <https://doi.org/10.1007/s11214-016-0292-x>
- Forget, F., Haberle, R. M., Montmessin, F., Levrard, B., & Head, J. W. (2006). Formation of glaciers on Mars by atmospheric precipitation at high obliquity. *Science*, *311*(5759), 368–371. <https://doi.org/10.1126/science.1120335>
- Forsberg-Taylor, N. K., Howard, A. D., & Craddock, R. A. (2004). Crater degradation in the Martian highlands: Morphometric analysis of the Sinus Sabaeus region and simulation modeling suggest fluvial processes. *Journal of Geophysical Research*, *109*, E05002. <https://doi.org/10.1029/2004JE002242>
- Golombek, M. P., Crumpler, L. S., Grant, J. A., Greeley, R., Cabrol, N. A., Parker, T. J., et al. (2006). Geology of the Gusev cratered plains from the Spirit rover traverse. *Journal of Geophysical Research*, *111*, E02S07. <https://doi.org/10.1029/2005JE002503>
- Golombek, M. P., Grant, J. A., Crumpler, L. S., Greeley, R., Arvidson, R. E., Bell, J. F. III, et al. (2006). Erosion rates at the Mars Exploration Rover landing sites and long-term climate change on Mars. *Journal of Geophysical Research, Planets*, *111*, E12S10. <https://doi.org/10.1029/2006JE002754>
- Golombek, M. P., Grott, M., Kargl, G., Andrade, J., Marshall, J., Warner, N., et al. (2018). Geology and physical properties investigations by the InSight Lander. *Space Science Reviews*, *214*(5), 84. <https://doi.org/10.1007/s11214-018-0512-7>
- Golombek, M. P., Kipp, D. M., Warner, N. H., Daubar, I. J., Ferguson, R. L., Kirk, R. L., et al. (2017). Selection of the InSight landing site. *Space Science Reviews*, *211*(1–4), 5–95. <https://doi.org/10.1007/s11214-016-0321-9>
- Golombek, M. P., Robinson, K., McEwen, A., Bridges, N., Ivanov, B., Tornabene, L., & Sullivan, R. (2010). Constraints on ripple migration at Meridiani Planum from opportunity and HiRISE observations of fresh craters. *Journal of Geophysical Research, Planets*, *115*, E00F08. <https://doi.org/10.1029/2010JE003628>
- Golombek, M. P., Warner, N. H., Ganti, V., Lamb, M. P., Parker, T. J., Ferguson, R. L., & Sullivan, R. (2014). Small crater modification on Meridiani Planum and implications for erosion rates and climate change on Mars. *Journal of Geophysical Research: Planets*, *119*, 2522–2547. <https://doi.org/10.1002/2014JE004658>
- Golombek, M. P., Warner, N. H., Grant, J. A., Hauber, E., Ansan, V., Weitz, C. M., et al. (2020). Geology of the InSight landing site on Mars. *Nature Communications*, *11*(1), 1014–1011. <https://doi.org/10.1038/s41467-020-14679-1>
- Grant, J. A., Arvidson, R. E., Crumpler, L. S., Golombek, M. P., Hahn, B., Haldemann, A. F. C., et al. (2006). Crater gradation in Gusev crater and Meridiani Planum, Mars. *Journal of Geophysical Research*, *111*, E02S08. <https://doi.org/10.1029/2005JE002465>
- Grant, J. A., Warner, N. H., Weitz, C. M., Golombek, M. P., Wilson, S. A., Baker, M., et al. (2020, This Issue). Modification of homestead hollow at the InSight landing site based on the distribution and properties of local deposits. *Journal of Geophysical Research*. <https://doi.org/10.1029/2019JE006350>
- Grant, J. A., Wilson, S. A., Cohen, B. A., Golombek, M. P., Geissler, P. E., Sullivan, R. J., et al. (2008). Degradation of Victoria crater, Mars. *Journal of Geophysical Research*, *113*, E11010. <https://doi.org/10.1029/2008JE003155>
- Hartmann, W. K. (1984). Does crater “saturation equilibrium” occur in the solar system? *Icarus*, *60*(1), 56–74. [https://doi.org/10.1016/0019-1035\(84\)90138-6](https://doi.org/10.1016/0019-1035(84)90138-6)
- Hartmann, W. K. (2005). Martian cratering 8: Isochron refinement and the chronology of Mars. *Icarus*, *174*(2), 294–320. <https://doi.org/10.1016/j.icarus.2004.11.023>
- Hartmann, W. K., & Neukum, G. (2001). Cratering chronology and the evolution of Mars. *Space Science Reviews*, *96*(1–4), 165–194. <https://doi.org/10.1023/A:1011945222010>
- Hartmann, W. K., & Daubar, I. J. (2016). Martian cratering 11. Utilizing decameter scale crater populations to study Martian history. *Icarus*, *5*, 565–576. <https://doi.org/10.1111/maps.12807>
- Head, J. W., Mustard, J. F., Krevslavsky, M. A., Milliken, R. E., & Marchant, D. R. (2003). Recent ice ages on Mars. *Nature*, *426*(6968), 797–802. <https://doi.org/10.1038/nature02114>
- Heimsath, A. M., Dietrich, W. E., Nishiizumi, K., & Finkel, R. C. (1999). Cosmogenic nuclides, topography, and the spatial variation of soil depth. *Geomorphology*, *27*(1–2), 151–172. [https://doi.org/10.1016/S0169-555X\(98\)00095-6](https://doi.org/10.1016/S0169-555X(98)00095-6)
- Heimsath, A. M., Dietrich, W. E., Nishiizumi, K., & Finkel, R. C. (2001). Stochastic processes of soil production and transport: Erosion rates, topographic variation and cosmogenic nuclides in the. *Oregon coast range*, *26*, 531–552.
- Hundal, C. B., Golombek, M. P., & Daubar, I. J. (2017). *Chronology of fresh rayed craters in Elysium Planitia, Mars*, 48th Lunar and Planetary Science, Abstract #1726. Houston: Lunar and Planetary Institute.
- Ivanov, B. A. (2001). Mars/moon cratering rate ratio estimates. *Space Science Reviews*, *96*(1/4), 87–104. <https://doi.org/10.1023/A:1011941121102>
- Jakosky, B. M., & Carr, M. H. (1985). Possible precipitation of ice at low latitudes of Mars during periods of high obliquity. *Nature*, *315*(6020), 559–561. <https://doi.org/10.1038/315559a0>
- Jakosky, B. M., & Christensen, P. R. (1986). Global duricrust on Mars: Analysis of remote-sensing data. *Journal of Geophysical Research*, *91*(B3), 3547–3559. <https://doi.org/10.1029/JB091iB03p03547>
- Jones, K. L., Arvidson, R. E., Guinness, E. A., Bragg, S. L., Wall, S. D., Carlston, C. E., & Pidek, D. G. (1979). One Mars year: Viking lander imaging observations. *Science*, *204*(4395), 799–806. <https://doi.org/10.1126/science.204.4395.799>
- Kedar, S., Andrade, J., Banerdt, B., Delage, P., Golombek, M., Grott, M., et al. (2017). Analysis of regolith properties using seismic signals generated by InSight’s HP3 penetrator. *Space Science Reviews*, *211*(1–4), 315–337. <https://doi.org/10.1007/s11214-017-0391-3>
- Kirk, R. L., Howington-Kraus, E., Rosiek, M. R., Anderson, J. A., Archinal, B. A., Becker, K. J., et al. (2008). Ultrahigh resolution topographic mapping of Mars with MRO HiRISE stereo images: Meter-scale slopes of candidate Phoenix landing sites. *Journal of Geophysical Research*, *113*, E00A24. <https://doi.org/10.1029/2007JE003000>

- Kneissl, T., van Gasselt, S., & Neukum, G. (2011). Map-projection-independent crater size-frequency determination in GIS environments – New software tool for ArcGIS. *Planetary and Space Science*, 59(11-12), 1243–1254. <https://doi.org/10.1016/j.pss.2010.03.015>
- Lognonné, P., Banerdt, W. B., Pike, W. T., Giardini, D., Christensen, U., Garcia, R. F., et al. (2020). Constraints on the shallow elastic and anelastic structure of Mars from InSight seismic data. *Nature Geoscience*, 13(3), 213–220. <https://doi.org/10.1038/s41561-020-0536-y>
- Madeleine, J. B., Head, J. W., Forget, F., Navarro, T., Millour, E., Spiga, A., et al. (2014). Recent ice ages on Mars: The role of radiatively active clouds and cloud microphysics. *Geophysical Research Letters*, 41, 4873–4879. <https://doi.org/10.1002/2014GL059861>
- Maki, J. N., Golombek, M., Deen, R., Abarca, H., Sorice, C., Goodsall, T., et al. (2018). The color cameras on the InSight lander. *Space Science Reviews*, 214(6), 1–34. <https://doi.org/10.1007/s11214-018-0536-z>
- Mangold, N., Adeli, S., Conway, S., Ansan, V., & Langlais, B. (2012). A chronology of early Mars climatic evolution from impact crater degradation. *Journal of Geophysical Research, Planets*, 117, E04003. <https://doi.org/10.1029/2011JE004005>
- Martin-Torres, F. J., Zorzano, M.-P., Valentín-Serrano, P., Harri, A.-M., Genzer, M., Kemppinen, O., et al. (2015). Transient liquid water and water activity at Gale crater on Mars. *Nature Geoscience*, 8(5), 357–361. <https://doi.org/10.1038/ngeo2412>
- McEwen, A. S., Eliason, E. M., Bergstrom, J. W., Bridges, N. T., Hansen, C. J., Delamere, W. A., et al. (2007). Mars reconnaissance orbiter's high resolution imaging science experiment (HiRISE). *Journal of Geophysical Research*, 112, E05S02. <https://doi.org/10.1029/2005JE002605>
- Melosh, H. J. (1989). *Impact craters: A geologic process*, (pp. 76–85). London: Oxford University Press.
- Michael, G. G. (2013). Planetary surface dating from crater size-frequency distribution measurements: Multiple resurfacing episodes and differential isochron fitting. *Icarus*, 226(1), 885–890. <https://doi.org/10.1016/j.icarus.2013.07.004>
- Michael, G. G., Platz, T., Kneissl, T., & Schmedemann, N. (2012). Planetary surface dating from crater size-frequency distribution measurements: Spatial randomness and clustering. *Icarus*, 218(1), 169–177. <https://doi.org/10.1016/j.icarus.2011.11.033>
- Michael, G. G., & Neukum, G. (2010). Planetary surface dating from crater size–frequency distribution measurements: Partial resurfacing events and statistical age uncertainty. *Earth and Planetary Science Letters*, 294(3), 223–229.
- Mischna, M. A., & Richardson, M. I. (2005). A reanalysis of water abundances in the Martian atmosphere at high obliquity. *Geophysical Research Letters*, 32, L03201. <https://doi.org/10.1029/2004GL021865>
- Moore, H. J., Bickler, D. B., Crisp, J. A., Eisen, H. J., Gensler, J. A., Haldemann, A. F. C., et al. (1999). Soil-like deposits observed by sojourner, the pathfinder rover. *Journal of Geophysical Research*, 104(E4), 8729–8746. <https://doi.org/10.1029/1998JE900005>
- Mueller, N. T., et al. (2019). The HP3 radiometer on InSight. Ninth international conference on Mars, Pasadena, California - July 22-25, 2019, abstract #6194.
- Mutch, T. A., Arvidson, R. E., Binder, A. B., Guinness, E. A., & Morris, E. C. (1977). The geology of the Viking Lander 2 site. *Journal of Geophysical Research*, 82(28), 4452–4467. <https://doi.org/10.1029/J082i028p04452>
- Pan, L., et al. (2019). Crustal stratigraphy and heterogeneities of the first kilometers at the dichotomy boundary in western Elysium Planitia and implications for InSight lander. *Icarus*, 338. <https://doi.org/10.1016/j.icarus.2019.113511>
- Pelletier, J. D., & Cline, M. L. (2007). Nonlinear slope-dependent sediment transport in cinder cone evolution. *Geology*, 35(12), 1067–1070. <https://doi.org/10.1130/G23992A.1>
- Pike, R. J. (1974). Depth/diameter relations of fresh lunar craters: Revision from spacecraft data. *Geophysical Research Letters*, 1(7), 291–294. <https://doi.org/10.1029/GL001i007p00291>
- Pike, R. J. (1977). Size-dependence in the shape of fresh impact craters on the moon. In D. J. Roddy, & R. B. Merrill (Eds.), *Impact and explosion cratering*, (pp. 489–507). New York: Pergamon Press.
- Reiss, D., & Lorenz, R. D. (2016). Dust devil track survey at Elysium Planitia, Mars: Implications for the InSight landing sites. *Icarus*, 266, 315–330. <https://doi.org/10.1016/j.icarus.2015.11.012>
- Sibson, R. (1981). A brief description of natural neighbor interpolation. In V. Barnett (Ed.), *Interpreting multivariate data*, (pp. 21–36). New York: John Wiley & Sons.
- Spohn, T., Grott, M., Smrekar, S. E., Knollenberg, J., Hudson, T. L., Krause, C., et al. (2018). The heat flow and physical properties package (HP3) for the InSight mission. *Space Science Reviews*, 214(5), 2018. <https://doi.org/10.1007/s11214-018-0531-4>
- Sullivan, R., Arvidson, R., Bell, J. F. III, Gellert, R., Golombek, M., Greeley, R., et al. (2008). Wind-driven particle mobility on Mars: Insight from Mars Exploration Rover observations at “El Dorado” and surroundings at Gusev crater. *Journal of Geophysical Research*, 113, E06S07. <https://doi.org/10.1029/2008JE003101>
- Sweeney, J., Warner, N. H., Ganti, V., Golombek, M. P., Lamb, M. P., Ferguson, R., & Kirk, R. (2018). Degradation of 100-m-scale rocky ejecta craters at the InSight landing site on Mars and implications for surface processes and erosion rates in the Hesperian and Amazonian. <https://doi.org/10.1029/2018JE005618>
- Tanaka, K. L., Skinner, J. A. Jr., Dohm, J. M., Irwin, R. P. III, Kolb, E. J., Fortezzo, C. M., et al. (2014). Geologic map of Mars. *U.S. Geol. Surv. Sci. Invest. Map*, 3292. <https://doi.org/10.3133/sim3292>
- Vaniman, D. T., Bish, D. L., Chipera, S. J., Fialips, C. I., Carey, J. W., & Feldman, W. C. (2004). Magnesium sulphate salts and the history of water on Mars. *Nature*, 431(7009), 663–665. <https://doi.org/10.1038/nature02973>
- Warner, N. H., Golombek, M. P., Sweeney, J., Ferguson, R. L., Kirk, R. L., & Schwartz, C. (2017). Near surface stratigraphy and regolith production in southwestern Elysium Planitia, Mars: Implications for Hesperian–Amazonian terrains and the InSight lander mission. *Space Science Reviews*, 211(1-4), 147–190. <https://doi.org/10.1007/s11214-017-0352-x>
- Warner, N. H., Gupta, S., Calef, F. J., Grindrod, P., & Goddard, K. (2015). Minimum effective area for high resolution crater counting of Martian terrains. *Icarus*, 245, 198–240. <https://doi.org/10.1016/j.icarus.2014.09.024>
- Warner, N. H., Gupta, S., Lin, S.-Y., Kim, J.-R., Muller, J.-P., & Morley, J. (2010). Late Noachian to Hesperian climate change on Mars: Evidence of episodic warming from transient crater lakes near Ares Vallis. *Journal of Geophysical Research*, 115, E06013. <https://doi.org/10.1029/2009JE003522>
- Watters, W. A., Geiger, L. M., Fendrock, M. A., & Gibson, R. (2015). Morphometry of small recent impact craters on Mars: Size and terrain dependence, short-term modification. *Journal of Geophysical Research: Planets*, 120, 226–254. <https://doi.org/10.1002/2014JE004630>
- Weitz, C. M., Grant, J. A., Warner, N. H., Golombek, M. P., Wilson, S. A., Hauber, E., et al. (2019). Clast sizes and shapes at the InSight landing site. 50th Lunar and Planetary Science, Abstract #1392.
- Williams, N. R., Golombek, M. P., Warner, N. H., Daubar, I. J., Hausmann, R. B., Hauber, E., et al. (2019). Surface alteration from landing InSight on Mars and its implications for shallow regolith structure. 50th Lunar and Planetary Science, Abstract #2781.
- Xie, M., Zhu, M.-H., Xiao, Z., Wu, Y., & Zu, A. (2017). Effect of topography degradation on crater size-frequency distributions: Implications for populations of small craters and age dating. *Geophysical Research Letters*, 44, 10,171–10,179. <https://doi.org/10.1002/2017GL075298>
- Yen, A. S., Gellert, R., Schröder, C., Morris, R. V., Bell JF 3rd, Knudson, A. T., et al. (2005). An integrated view of the chemistry and mineralogy of martian soils. *Nature*, 436(7047), 49–54. <https://doi.org/10.1038/nature03637>